Atmos. Chem. Phys. Discuss., 15, 29871–29937, 2015
www.atmos-chem-phys-discuss.net/15/29871/2015/
doi:10.5194/acpd-15-29871-2015

Atmospheric Chemistry and Physics Discussions

Carbon monoxide climatology derived from the trajectory mapping of global MOZAIC-IAGOS data

M. Osman[1], D. W. Tarasick[1], J. Liu[2], O. Moeini[1], V. Thouret[3], V. E. Fioletov[1], M. Parrington[4], and P. Nédélec[3]

[1]Environment Canada, 4905 Dufferin Street, Downsview, ON, M3H 5T4, Canada
[2]Department of Geography and Program in Planning, University of Toronto, 100 St. George Street, Toronto, Ontario, M5S 3G3, Canada
[3]Laboratoire d'Aérologie, UMR5560, CNRS and Université de Toulouse, Toulouse, France
[4]European Centre for Medium-Range Weather Forecasts, Shinfield Park, Reading, RG2 9AX, UK

Received: 17 September 2015 – Accepted: 12 October 2015 – Published: 2 November 2015

Correspondence to: D. W. Tarasick (david.tarasick@ec.gc.ca)

Published by Copernicus Publications on behalf of the European Geosciences Union.

Abstract

A three-dimensional gridded climatology of carbon monoxide (CO) has been developed by trajectory mapping of global MOZAIC-IAGOS in situ measurements from commercial aircraft data. CO measurements made during aircraft ascent and descent, comprising nearly 41 200 profiles at 148 airports worldwide from December 2001 to December 2012 are used. Forward and backward trajectories are calculated from meteorological reanalysis data in order to map the CO measurements to other locations, and so to fill in the spatial domain. This domain-filling technique employs 15 800 000 calculated trajectories to map otherwise sparse MOZAIC-IAGOS data into a quasi-global field. The resulting trajectory-mapped CO dataset is archived monthly from 2001–2012 on a grid of 5° longitude × 5° latitude × 1 km altitude, from the surface to 14 km altitude.

The mapping product has been carefully evaluated, by comparing maps constructed using only forward trajectories and using only backward trajectories. The two methods show similar global CO distribution patterns. The magnitude of their differences is most commonly 10 % or less, and found to be less than 30 % for almost all cases. The trajectory-mapped CO dataset has also been validated by comparison profiles for individual airports with those produced by the mapping method when data from that site are excluded. While there are larger differences below 2 km, the two methods agree very well between 2 and 10 km with the magnitude of biases within 20 %.

Maps are also compared with Version 6 data from the Measurements Of Pollution In The Troposphere (MOPITT) satellite instrument. While agreement is good in the lowermost troposphere, the MOPITT CO profile shows negative biases of ∼ 20 % between 500 and 300 hPa. These upper troposphere biases are not related to the mapping procedure, as almost identical differences are found with the original in situ MOZAIC-IAGOS data. The total CO trajectory-mapped MOZAIC-IAGOS climatology column agrees with the MOPITT CO total column within ±5 %, which is consistent with previous reports.

ACPD
15, 29871–29937, 2015

The maps clearly show major regional CO sources such as biomass burning in the central and southern Africa and anthropogenic emissions in eastern China. The dataset shows the seasonal CO cycle over different latitude bands and altitude ranges that are representative of the regions as well as long-term trends over latitude bands. We observe a decline in CO over the Northern Hemisphere extratropics and the tropics consistent with that reported by previous studies.

Similar maps have been made using the concurrent O_3 measurements by MOZAIC-IAGOS, as the global variation of O_3–CO correlations can be a useful tool for the evaluation of ozone sources and transport in chemical transport models. We anticipate use of the trajectory-mapped MOZAIC-IAGOS CO dataset as an a priori climatology for satellite retrieval, and for air quality model validation and initialization.

1 Introduction

Atmospheric carbon monoxide (CO) is an important global air pollutant and trace gas. Due to its relatively long lifetime of 1–4 months (Hubler et al., 1992; Law and Pyle, 1993), it is an ideal tracer for long range atmospheric transport (Logan et al., 1981; Lelieveld et al., 2001; Shindell et al., 2006). Moreover, in the tropics, it is an important tracer of upward transport during convective events (e.g., Pommrich et al., 2014). Consequently, it has been employed to facilitate interpretations of chemical measurements (Jaffe et al., 1996; Parrish et al., 1991, 1998; Wang et al., 1996, 1997) and in validating chemical transport models (Carmichael et al., 2003; Liu et al., 2003; Tan et al., 2004; Wang et al., 2004). The main sources of atmospheric CO are relatively well understood (Galanter et al., 2000; Granier et al., 2011; Holloway et al., 2000); however, the magnitude of individual sources and their seasonal variability, especially of biomass burning, are not well quantified. Stein et al. (2014) also reported that models are also generally biased low due to either an underestimation of CO sources or an overestimation of its sinks. There are differences in the emission densities of anthropogenic and natural sources, despite the fact that the anthropogenic and natural sources are

ACPD
15, 29871–29937, 2015

of similar magnitude on a global scale (Granier et al., 2011; Logan et al., 1981). The anthropogenic sources are primarily associated with large industrial centers or major biomass burning regions while the natural sources, such as oxidation of methane (CH_4) and non-methane hydrocarbons (NMHCs) are much more diffuse. This makes CO a good atmospheric tracer gas for anthropogenic emissions as its lifetime allows it to be used as an indicator of how large-scale atmospheric transport redistributes pollutants on a global scale.

CO plays a vital role in the chemistry of the atmosphere. This significance mainly comes from the influence of CO on the concentrations and distributions of the atmospheric oxidants, ozone (O_3), the hydroperoxy (HO_2) and hydroxyl radicals (OH) (e.g. Novelli et al., 1994, 1998). Reaction (R1) between CO and OH represents 90–95 % of the CO sink (Logan et al., 1981), and about 75 % of the removal of OH (Thompson, 1992) in the troposphere:

$$CO + OH \rightarrow CO_2 + H \quad \text{(R1)}$$

$$H + O_2 \rightarrow HO_2 + M \quad \text{(R2)}$$

In areas with sufficient NO_x ($= NO + NO_2$), HO_2 formed in Reaction (R2) leads to photochemical Reactions (R3)–(R5) which bring about net O_3 production. In urban areas and regions of biomass burning, large amounts of these O_3 precursors will be produced, and O_3 can be formed in, and downwind of, the source region (Crutzen, 1973; Fishman and Seiler, 1983):

$$HO_2 + NO \rightarrow OH + NO_2 \quad \text{(R3)}$$

$$NO_2 + h\nu \rightarrow NO + O(< 425\,\text{nm}) \quad \text{(R4)}$$

$$O_2 + O + M \rightarrow O_3 \quad \text{(R5)}$$

O_3 is associated with respiratory problems and decreased crop yields (e.g., McKee, 1993; Chameides et al., 1994). Since CO and OH are principal reaction partners, CO concentrations in the atmosphere have important climatological implications. OH is also responsible for the removal of greenhouse gases such as CH_4, and other volatile

ACPD
15, 29871–29937, 2015

organic compounds in the atmosphere. Via these interactions with OH, O_3 and CH_4, CO has an indirect radiative forcing of about 0.25 $W m^{-2}$ (IPCC AR5).

Global atmospheric chemistry models require accurate CO concentrations on a global scale in order to define spatial and temporal variations of atmospheric oxidants and CO. For this reason measurements of CO are made by different kinds of remote sensing and in situ instruments, in ground-based networks, aircraft programmes and from space (Novelli et al., 1994, 1998; Rinsland and Levine, 1985; Zander et al., 1989; Brook et al., 2014; Reichle et al., 1990, 1999; Worden et al., 2013; Petzold et al., 2015). Background CO levels are found in all regions of the troposphere, where mixing ratios between 45 and 250 ppbv have been reported (Novelli et al., 1994). Extreme mixing ratios much higher than 250 ppb have been observed in the upper troposphere over Asia (Nédélec et al., 2005) or over the Pacific (Clark et al., 2015) in plumes of boreal biomass burning. The largest values in the lower troposphere have been observed over Beijing (Zbinden et al., 2013).

Early studies of ground-based observations showed increasing trends in global CO before 1980 (Khalil and Rasmussen, 1988; Rinsland and Levine, 1985; Zander et al., 1989), followed by a modest decline in the 1990s (Novelli et al., 1994, 2003; Khalil and Rasmussen, 1994). More recently satellite observations have shown that the decline has continued: Worden et al. (2013) report a global trend from 2000–2011 of $\sim 10\,\%\,decade^{-1}$ on column CO in the Northern Hemisphere. Petetin et al. (2015) show a similar decrease of about 2 $ppb\,year^{-1}$ over Frankfurt throughout the troposphere from 2002 to 2012. The decrease is at least partly due to a decrease in global anthropogenic CO emissions (Granier et al., 2011).

In-service Aircraft for a Global Observing System (IAGOS), and its predecessor Measurement of OZone and water vapor by AIrbus in-service airCraft (MOZAIC), have been making automatic and regular measurements of O_3, water vapour and standard meteorological parameters onboard long-range commercial Airbus A340 aircraft since August 1994 (Marenco et al., 1998; Petzold et al., 2015). Measurements of CO (Nédélec et al., 2003) and NO_y (Volz-Thomas et al., 2005) were added in late 2001.

ACPD
15, 29871–29937, 2015

The MOZAIC database currently contains data from more than 71 900 vertical profiles of O_3 and 41 200 vertical profiles of CO, measured during takeoff and landing from 148 airports around the world. MOZAIC measurements show the general features of the atmospheric CO distribution (Zbinden et al., 2013; Petzold et al., 2015 and references therein), capturing major regional features (e.g., strong CO emissions from biomass burning or anthropogenic sources).

The objective of this paper is to present a three-dimensional (i.e., latitude, longitude, altitude) gridded climatology of carbon monoxide that has been developed by trajectory mapping of global MOZAIC-IAGOS CO data from 2001–2012. We employ a domain-filling technique, using approximately 15 800 000 calculated trajectories to map otherwise sparse MOZAIC-IAGOS CO data into a global field.

This is a technique that has been used successfully with tropospheric and stratospheric ozonesonde data (G. Liu et al., 2013; J. Liu et al., 2013). Stohl et al. (2001) used trajectory statistics to extend one year of MOZAIC O_3 measurements into a 4-season O_3 climatology at 10° longitude by 6° latitude and three vertical heights. Tarasick et al. (2010) developed high resolution (1° × 1° × 1 km in latitude, longitude, and altitude) tropospheric O_3 fields for North America from ozonesonde data from the INTEX (Intercontinental Transport Experiment) and ARCTAS (Arctic Research of the Composition of the Troposphere from Aircraft and Satellites) campaigns, and this was extended to global tropospheric ozonesonde data by G. Liu et al. (2013). It is possible to apply this technique to CO because the lifetime of CO in the troposphere, as noted above, is generally of the order of weeks or months. This physically-based interpolation method, using the reanalysis meteorological data from the National Centers for Environmental Prediction/National Center for Atmospheric Research (NCEP/NCAR) (Kalnay et al., 1996), offers obvious advantages over typical statistical interpolation methods. Indeed, it is expected to improve global models and satellite data validation and it can also be used as a priori for satellite data retrieval.

Major regional features of the global CO distribution are clearly evident in the global maps thus produced, especially regions of intense biomass burning or anthropogenic

ACPD
15, 29871–29937, 2015

pollution. The 3-D global trajectory-mapped CO climatology facilitates visualization and comparison of different years, decades, and seasons, and offers insight into the global variation of CO. Moreover, it will be useful for climate and air quality model initialization and validation, and can be used as an a priori climatology for satellite data retrievals. Comparison with similar maps made using the concurrent O_3 measurements by MOZAIC-IAGOS allow us to examine the global variation of O_3–CO correlations, which convey information about the source distribution of CO.O_3–CO correlations are also of great interest around the tropopause region since such correlations provide information on mixing processes (e.g., Hoor et al., 2004; Pan et al., 2006; Vogel et al., 2011) besides of the source regions. This paper is organized in the following order. Following discussion of the MOZAIC-IAGOS and MOPITT instruments in Sects. 2.1 and 2.2, respectively, we describe trajectory mapping calculation via HYSPLIT model in Sect. 2.3. The transformtion of MOZAIC-IAGOS data by applying the MOPITT a priori profile and averaging kernels is presented in Sect. 2.4. The validation of the trajectory-mapped dataset against MOZAIC-IAGOS in situ data will be presented in Sect. 3. The same section assesses the differences between the CO mapping produced using only backward and only forward trajectories, and also compares with in situ global CO data at cruise altitudes between 8 and 12 km. Subsequently, the comparison of the trajectory-mapped MOZAIC-IAGOS CO with MOPITT CO retrievals is presented in Sect. 4. Section 5 discusses the results obtained from the global 3-D trajectory-mapped climatology data. After pointing out the potential applications of the trajectory-mapped MOZAIC-IAGOS CO climatology (i.e., O_3–CO relationship and global variation and trends of CO) in Sect. 6, we make concluding remarks about the results we obtain from this study in Sect. 7.

ACPD
15, 29871–29937, 2015

2 Measurements of CO

2.1 MOZAIC-IAGOS

CO measurements were made by an improved version of a commercial Model 48CTL CO Analyzer from Thermo Environmental Instruments employing the Gas Filter Correlation technique. The Model 48CTL is based on the principle that CO absorbs infrared radiation at a wavelength of 4.67 microns. For 30 s integration time (the response time of the instrument) the precision achieved is 5 ppb (noise) or 5 % (calibration) CO, with minimum detection limit of 10 ppb. The analyzer samples at a horizontal resolution of about 7 km (since the maximum cruise speed of the Airbus A340 aircraft is nearly 250 $\mathrm{m\,s^{-1}}$) and the vertical resolution during ascents and descents is nearly 300 m. Nedelec et al. (2003 for MOZAIC, 2015 for IAGOS) give detailed descriptions of the CO analyzer, measurement technique, instrument validation and quality testing.

The airports visited by aircraft equipped with MOZAIC-IAGOS instrumentation are shown in Fig. 1. Further details are available at http://www.iagos.fr.

The sampled data from these airports are unevenly distributed both spatially and temporally because the frequency of visits to airports by aircraft that take part in MOZAIC-IAGOS varies considerably depending on commercial airlines' operational constraints. This means that at airports such as Frankfurt, Germany we find as many as 12 324 CO profiles while from Dammam, Saudi Arabia we have only 2 CO profiles during the period 2001–2012. The trajectory-mapping method is valuable for filling the sparse and variable spatial domain.

2.2 MOPITT

MOPITT is a nadir-viewing gas correlation radiometer which provides global atmospheric profiles of CO volume mixing ratio (VMR) and CO total column values using near-infrared radiation at 2.3 µm and thermal-infrared radiation at 4.7 µm. CO columns and profiles are retrieved from the IR emission channels (4.6 µm) for all cloud-free

ACPD
15, 29871–29937, 2015

scenes. The MOPITT measurement technique relies on thermal contrast between the Earth's surface and atmosphere, leading to a retrieval dependence on surface temperature, and little sensitivity to CO in the boundary layer. The retrieval uses a priori profiles that vary geographically and temporally. MOPITT-derived CO VMR profiles reflect the vertical sensitivity of the measurement as defined by the retrieval averaging kernel (e.g. Fig. 2) and a priori profile. In this study, we have used Level 3, Version 6 monthly CO mixing ratio profile data, reported on 10 pressure levels, as well as CO total column. MOPITT data are publicly available at the NASA Langley Research Center Atmospheric Science Data Center: https://eosweb.larc.nasa.gov/project/mopitt/mopitt_table.

MOPITT was launched in 1999 into sun-synchronous polar orbit with a 1030 local time (LT) northward or southward local equator cross-over time. The instrument field of view is 22 km × 22 km. Cross-track scanning with a 612 km swath provides near complete coverage of the surface of the Earth approximately every 3 days. MOPITT retrievals have gone through intensive validation against in situ measurements from aircraft on a regular basis since the start of the mission (Worden et al., 2010; Deeter et al., 2012, 2013, 2014; Emmons et al., 2004, 2007, 2009; Jacob et al., 2003). MOPITT CO retrievals have also been validated by comparing to ground-based and TES satellite measurements (Jacob et al., 2003 and Lou et al., 2007). In the lower troposphere a mean positive bias of 6–8 % against in situ validation profiles has been reported, and a mean bias and standard deviation for the retrieved CO column of 5 ± 11 and -0.5 ± 12.1 % for periods, respectively, March 2000–May 2001 and August 2001–December 2002 (Emmons et al., 2004). Jacob et al. (2003) reported the CO bias to be 6 ± 2 %, where as Emmons et al. (2007) found approximately 7 ± 8 % bias for summer 2004 measurements. Deeter et al. (2013) also show a total column retrieval bias of about 0.08×10^{18} molecules cm^{-2} (~ 4 %) against in situ profiles. Furthermore, Deeter et al. (2012) reported a positive bias of surface-level CO concentrations on the order of a few percent against in situ profiles.

ACPD
15, 29871–29937, 2015

2.3 Trajectory calculation and global CO mapping via HYSPLIT

For each CO profile of the MOZAIC-IAGOS data set presented here, the mean CO VMR was calculated for 1 km intervals from sea level up to 12 km (the maximum altitude of the aircraft). Cruise data were not used. The HYSPLIT (Hybrid Single-Particle Lagrangian Integrated Trajectory) model version 4.9 (Draxler and Hess, 1998; Draxler, 1999) was employed to calculate trajectories for each level of each profile. HYSPLIT, publicly accessible at (http://ready.arl.noaa.gov/HYSPLIT.php), uses the reanalysis meteorological wind fields from the National Centers for Environmental Prediction/National Center for Atmospheric Research (NCEP/NCAR) (Kalnay et al., 1996) as an input to describe the transport of CO in the atmosphere. The reanalysis data are readily available from 1948 until the present. Both forward and backward trajectories for 4 days at 6 h intervals (32 positions for each level) were calculated for 41 200 CO profiles, and the mean CO mixing ratios from each level (i.e., tropospheric and lower stratospheric air masses) of each profile were assigned to the corresponding trajectory positions along the forward and backward paths. Trajectories only move upward and downward with the meteorological vertical velocity fields since the HYSPLIT kinematic trajectory model employs vertical motions supplied with the NCEP reanalysis meteorological data set. Numerous studies show that the choice of vertical wind velocity has significant impact on the transport of tracers (e.g., Schoeberl et al., 2003; Ploeger et al., 2010, 2012). Kinematic models show excessive dispersion for tracers with strong gradients (e.g., O_3 in the vicinity of the tropopause), particularly for trajectories of 7 days or more. We limit trajectories to a maximum for 4 days in length. Moreover, unlike O_3, CO does not have strong vertical gradient in the upper troposphere. Trajectories that reach the bottom boundary (i.e., ground) continue at the surface where the trajectory robustness grows to be more uncertain. Trajectories that reach the top height of the model (20 000 m a.s.l.) will terminate. Although HYSPLIT is capable of generating a trajectory every hour (i.e., 24 trajectories day^{-1}), the average available CO measurements (if the MOZAIC-IAGOS aircraft visits the airports) is around 2 profiles day^{-1} with the ex-

ACPD
15, 29871–29937, 2015

ception of Frankfurt where we can get up to 6 profiles day^{-1}. In this trajectory-mapped MOZAIC-IAGOS CO climatology, we did not exclude major anthropogenic CO sources; however, the climatology could in principle be refined by excluding backtrajectories from sources identified via emission inventories. We note, however, that if major anthropogenic sources were a significant source of error, we would see differences between the CO mapping produced using only backward and only forward trajectories (see Sect. 3.1).

This mapping implicitly assumes that CO chemistry may be neglected over a timescale of 4 days. Except near major anthropogenic sources, this assumption should be valid, as the lifetime of CO is much longer. However, trajectories have significant errors over such timescales. Stohl (1998) in a comprehensive review, quotes typical errors of about 100–200 km day^{-1} in the troposphere. This can be combined with an estimate of the correlation length in the troposphere to yield an estimate for the information value of a mapped measurement. Liu et al. (2009) find that O_3 measurements in the troposphere correlate with an exponential dependence of approximately $e^{-r^{1.5}}$ (with r shown in Eq. 1), and a correlation length of 500–1000 km in the troposphere, and 1000–2000 km in the stratosphere. The means that the horizontal distance for the correlation coefficient to decrease by a factor of e is 500–1000 km in the troposphere and 1000–2000 km in the stratosphere. As the CO lifetime is even longer than the ozone lifetime, the correlation length for CO should be at least as large. Therefore, the trajectory-mapped data were binned at intervals of 5° latitude and 5° longitude, at every 1 km altitude, and averaged with a weighting, w, assigned according to the formula:

$$w = e^{-(150t/R)^{1.5}} \quad (1)$$

where R is the correlation length (700 and 1500 km in the troposphere and stratosphere, respectively), and t is the age of the trajectory in days.

The trajectory mapping greatly spreads out the in situ CO information along the trajectory paths, increasing the spatial domain to include much of the globe. Two different vertical coordinate systems were utilized for the binning, and hence the maps were

ACPD
15, 29871–29937, 2015

generated for elevations above sea level and above ground level. Data are available publicly at ftp://es-ee.tor.ec.gc.ca/pub/ftpdt/. In this work, we present global CO maps generated for elevations above sea level. Global maps of monthly, annual, seasonal and decadal means are presented, for each altitude, from 2001–2012.

2.4 MOZAIC-IAGOS Comparison with MOPITT

When comparing the MOPITT retrievals with in situ data, it is necessary to take into account the sensitivity of the retrievals to the true profiles. The method used by MOPITT to retrieve tropospheric CO profiles follows that of Rodgers (2000). In order to perform the most meaningful and accurate comparison, the in situ data to be compared must be transformed using the averaging kernel matrix, **A**, and a priori profile, x_a, as shown by Eq. (2). A "retrieved" comparison profile, x_{ret}, is calculated by using the in situ profile, x, as the "true" profile in Eq. (2) which is interpolated to the lower resolution of MOPITT. As described by Emmons et al. (2004), the in situ profile (x) is transformed with averaging kernel matrix (**A**) and the a priori CO profile (x_a) to get a profile (x_{ret}), the appropriate quantity to compare with the MOPITT retrievals:

$$x_{ret} = x_a + \mathbf{A}(x - x_a) = \mathbf{A}x + (\mathbf{I} - \mathbf{A})x_a \quad (2)$$

where **I** is the identity matrix. The averaging kernels provide the relative weighting between the true and a priori profiles and reflect the sensitivity of the retrieval to the measurement. They are very sensitive to the surface temperature and will be different for each point on the globe. The matrix **A** describes the sensitivity of the retrieved CO log(VMR) profile to perturbations applied at each level of the "true" log(VMR) profile. The quantity x_{ret}, the transformed in situ profile, represents the result of applying a linear transformation to the in-situ profile in the same way that the remote sensing retrieval process is believed to transform the true profile. Thus, x_{ret} can be directly compared against the MOPITT retrieved CO profile in a manner that is not affected by varying vertical resolution or a priori dependence. x_{ret}, x, and x_a are expressed in terms of the natural/common logarithm of the volume mixing ratio (VMR), i.e., $\log_e(\mathrm{VMR})/\log_{10}(\mathrm{VMR})$.

ACPD
15, 29871–29937, 2015

The vertical resolution of the retrieved profile is described by the shapes of the averaging kernels. Figure 2 shows that the kernels are broad except at pressure levels between 400–300 hPa and exhibit a large degree of overlap. The overlap of the averaging kernels peaking in the boundary layer and those at the top of the atmosphere indicates a significant correlation for the retrieved values at these levels. The retrieved CO values at these levels are also influenced by CO at mid levels, and by the a priori CO profile at all pressure levels. The averaging kernels describe the relative contributions, to the CO VMR retrieved at a given level, of the true and a priori (via $\mathbf{I} - \mathbf{A}$) CO profiles at all pressure levels (Eq. 2). Where the area under the averaging kernel is smaller, the a priori information in the retrieved CO profile is relatively larger. MOPITT CO averaging kernels exhibit variability from month to month, season to season as well as nighttime to daytime, depending on the atmospheric temperature profile, surface pressure and the CO profile itself.

The vertical coordinate of the MOZAIC-IAGOS climatology profile is km a.s.l., while the MOPITT a priori profile and averaging kernels are on pressure levels in hPa. Therefore, before applying the MOPITT averaging kernels the climatology data were interpolated using NCEP global pressure profiles that vary as a function of time (month) and latitude, to the 10 vertical pressure grid levels (1000, 900, 800, 700, 600, 500, 400, 300, 200, and 100 hPa) used by MOPITT. The interpolated profile was then convolved with the a priori profile and the averaging kernels following Eq. (2) (Emmons et al., 2004). For the atmospheric residual above the maximum MOZAIC-IAGOS profile altitude, the MOPITT a priori profiles were used.

In order to compare with these transformed CO profiles, the MOPITT CO profiles, averaging kernels, and a priori profiles were mapped down from the original horizontal resolution of $1^\circ \times 1^\circ$ in latitude and longitude to a reduced $5^\circ \times 5^\circ$ grid. The mapping was linear in log pressure and volume mixing ratio of CO. An example of comparisons of trajectory-mapped MOZAIC-IAGOS CO profiles with an individual (reduced) $5^\circ \times 5^\circ$ MOPITT CO profiles is shown in Fig. 2. The original trajectory-mapped MOZAIC-IAGOS CO profile, the a priori profile, and the transformed trajectory-mapped

ACPD
15, 29871–29937, 2015

MOZAIC-IAGOS CO profile are shown along with the MOPITT retrieved CO profile. The application of the averaging kernels to the MOZAIC-IAGOS CO profile results in significant vertical transformation, which can shift mixing ratios significantly at some levels. The averaging kernel, for example, identified as "1000" (i.e., surface) shows how changes to the true CO mixing ratio at all ten retrieval levels would each contribute to a change in the retrieved value at the surface at 1000 mbar. The original trajectory-mapped MOZAIC-IAGOS climatology profile is quite different from the transformed climatology profile and as seen from the same figure the departures of the transformed CO mixing ratio from the true mixing ratios can be as large as 60 ppb at some pressure levels.

3 Validation

Validation of the trajectory-mapped MOZAIC-IAGOS CO dataset product has been performed by Eq. (1) comparing maps constructed using only forward trajectories against with those constructed using only backward trajectories, and Eq. (2) comparing profiles for individual airports against those produced by the mapping method when data from that site are excluded. The airport stations that have been selected in this validation study represent tropical and Northern Hemisphere midlatitude locations that are subject to different meteorological and CO source conditions.

3.1 Comparison of trajectory-mapped MOZAIC-IAGOS CO profiles

As a first step in validation of the trajectory-mapped climatology, Figs. 3 and S1 (in the Supplement) assess the differences between the CO mapping produced using only backward and only forward trajectories for different seasons using the 7.5 km level as an example. If chemistry (i.e. local sources or sinks) were a significant source of error then one would expect to see differences between these maps. In fact, the CO distribution patterns are very similar (Fig. 3). Differences are most commonly 10 % or less, and

ACPD
15, 29871–29937, 2015

found to be less than 30 % for almost all cases. They are typically less than 10 % at northern mid-latitudes and less than 20 % in the tropics between ± 30° latitude, except in the Pacific and Atlantic oceans where they can be as large as 30 %. As Fig. S1 illustrates, differences also show no distinct pattern, except for some clustering in areas where the trajectories are longest, and therefore least reliable. As differences between the two distributions are comparable with the uncertainties of the mean value estimates and not systematic, it is reasonable to combine forward and backward mapped values to produce an averaged CO map.

3.2 Comparison between trajectory-mapped and in situ profiles

A good test of an interpolation model is to examine how it performs in areas where no data are available. Figure 4 compares the trajectory-mapped climatology profiles at three airport sites (Frankfurt, Germany; Houston, USA; and Tokyo, Japan) with the average of the MOZAIC-IAGOS data from each of these sites for May of 2001–2012. However, since the sampling frequency varies from airport to airport, Houston and Tokyo are not as well sampled as Frankfurt throughout the period. The climatology profiles for each location were produced by excluding data from that location, but using all other MOZAIC-IAGOS data.

Generally, the profiles from the two methods agree very well and the agreement is especially good in the free troposphere, at altitudes between 2 and 10 km. Referring to the bottom panels of Fig. 4, the magnitude of the differences for most altitudes is well under 20 %.

In Fig. 5 we extend the comparisons shown in Fig. 4 for other seasons as well as for another airports that represent different meteorological and source conditions. The selected airports are Atlanta (USA), Cairo (Egypt), Frankfurt (Germany), Houston (USA), Khartoum (Sudan), Lagos (Nigeria), Los Angeles (USA), Nagoya (Japan), New Delhi (India), New York (USA), Tel Aviv (Israel) and Tokyo (Japan). Again, the sampling frequency among the airports is not the same throughout the period. Similar to the results shown in Fig. 4, in Fig. 5 we notice good agreement between the trajectory-mapped

ACPD
15, 29871–29937, 2015

and the in situ measurements for different locations and seasons across the globe. There are larger differences below 2 km where trajectories have larger errors predominantly due to complex dispersion and turbulence in the planetary boundary layer (Stohl and Seibert, 1998). However, the overall agreement between 2 and 10 km is very good with biases again within 20 %. As in previous studies using this method, the largest differences are seen where other sources of data are distant. The smallest overall bias is seen at Frankfurt, even though the exclusion of Frankfurt data removes nearly 1/3 of the total number of profiles. Apparently data from nearby airports such as Munich (Germany) and Brussels (Belgium) map accurately to the Frankfurt location. The consistency of these validation tests suggests that the trajectory-mapped dataset provides a reliable picture of the tropospheric CO distribution.

3.3 Comparison with the MOZAIC-IAGOS in-situ for upper troposphere

We can also compare the trajectory-mapped profile data and MOZAIC-IAGOS in situ global CO data at cruise altitudes between 8 and 12 km. The maps found at http://www.iagos.fr/macc/reanalysis_climatology_CO.php show the global seasonal mean (December–February, March–May, June–August and September–November) distribution of CO in the upper troposphere (within 60 hPa below the tropopause) for the period from 2003 to 2011. The figure clearly shows the seasonal cycle of CO with seasonal maximum in the Northern Hemisphere (NH) spring (MAM) and peak CO values in the Southern Hemisphere (SH) spring (SON). Elevated CO levels in the upper troposphere are generally seen over the areas where there is strong biomass burning. The figure also reveals high CO emissions are observed over eastern China in MAM primarily due to a rise in coal use (Boden et al., 2009; Gregg et al., 2008; Tie et al., 2006) and a increasing number of vehicles (Cai and Xie, 2007).

Figure 6 shows the trajectory-mapped global seasonal variation of CO for December–February, March–May, June–August and September–November 2001–2012 at altitudes between 7 and 9 km a.s.l. The trajectory-mapping yields more data over the oceans and NH high latitudes in Fig. 6 than is seen in CO maps cited above.

ACPD
15, 29871–29937, 2015

However, major regional features of the global CO distributions for different seasons are clearly evident in both figures. The figures show seasonal high CO values in spring in both hemispheres and elevated CO levels over regions where there is intensive biomass burning (central Africa, southern Africa and South America) and anthropogenic emissions (eastern China). Comparable CO values are noticeable from the figures over the Northern Atlantic Ocean as well as Greenland. Such an overall good qualitative agreement between the trajectory-mapped CO and MOZAIC-IAGOS in situ CO cruise data result suggests that the trajectory-mapped CO dataset performs well in remote areas as well.

4 Trajectory-mapped MOZAIC-IAGOS Versus MOPITT

This section is devoted to comparing the trajectory-mapped MOZAIC-IAGOS CO dataset with the extensively validated product from the MOPITT instrument onboard the NASA Terra satellite, which has been operating continuously since March 2000 (Drummond and Mand, 1996; Edwards et al., 1999). Global comparison was made for both CO profiles and CO total column for different time periods.

4.1 Comparison with MOPITT CO profiles

As described in Sect. 2.4, in order to make a rigorous comparison with MOPITT data, the climatology profiles are first transformed using the corresponding MOPITT a priori profiles and averaging kernels via Eq. (2). Figure 2 shows examples of retrieved CO profiles (x_{ret}), together with the original climatology (x) and the a priori profiles (x_{a}).

When examining the comparison between the MOPITT CO retrieval and the trajectory-mapped CO profile it is useful to keep in mind the shapes of the averaging kernels. For example, the 100 and 1000 mbar kernels are typically less peaked than the other pressure levels. Consequently, the generally broad and weak averaging kernel demonstrates that a significant fraction of the information used in the retrieval is

ACPD
15, 29871–29937, 2015

from the a priori profile or CO from other layers or both. Figure 2 also cautions that the transformed trajectory-mapped MOZAIC-IAGOS CO is closer to both the MOPITT CO retrievals and a priori profiles when there is less information from the measurement. Furthermore, as can be seen from Fig. 2, the MOPITT retrievals are not able to resolve the finer scale vertical structure of the trajectory-mapped CO profiles. The departures of the retrieved CO VMR from the trajectory-mapped VMRs at some pressure levels are as large as 60 ppb. In the lower troposphere the MOPITT CO retrieval profile is positively biased whereas the bias is negative in the upper troposphere. In Fig. 2, we have used only the dayside retrievals from MOPITT as the dayside retrievals have the maximum information content (Deeter et al., 2004). The MOPITT V6 L3 retrievals are used in this analysis.

Figure 7 shows profile comparisons between MOPITT retrievals and the MOZAIC-IAGOS climatology for global CO data at pressure levels 900, 700, 500, and 300 hPa. The slopes and correlations between MOPITT CO retrievals and the CO climatology (after applying the averaging kernels and the a priori profiles) for different levels are indicated in the figure. The different dot colors shown in Fig. 7 stand for different latitude bands: 23.5–66.5° S (SH extratropics), 23.5° S–23.5° N (tropics), 23.5–66.5° N (NH extratropics). The same figure shows that there are clearly two distinct clusters of dots in Fig. 7a and b and the high CO VMRs values seen here are from tropics with a very few from the NH extratropics. The enhanced CO values may have originated from anthropogenic sources and/or biomass burning; however, identifying individual sources is beyond the scope of this paper. Recent work by Ding et al. (2015) shows the association of enhanced CO in the free troposphere with the uplifting of CO from biomass burning and anthropogenic sources.

MOPITT and trajectory-mapped MOZAIC-IAGOS CO climatology mixing ratios are well-correlated with correlation coefficients of 0.7 or higher, for daytime data over both land and ocean. However, Fig. 7 also reveals significant biases between MOPITT retrievals and the trajectory-mapped MOZAIC-IAGOS CO climatology above 700 hPa.

ACPD
15, 29871–29937, 2015

Although in Fig. 7 we have chosen to show biases for January 2001–2012, the same analysis for other months and time periods yields similar results.

MOPITT seems to underestimate CO VMR by as much as 21 % against the trajectory-mapped MOZAIC-IAGOS CO climatology at 500 hPa. This result is significantly different from previous work such as Deeter et al. (2014, 2013, 2010) and Emmons et al. (2004, 2007, 2009). Most of these examined earlier versions of the MOPITT L3 product, although Deeter et al. (2014) use the MOPITT L3 V6 product, and reported biases varying from −5.2 % at 400 hPa to 8.9 % at the surface. In all cases the validation data consisted of flask samples taken by NOAA aircraft. In order to eliminate the possibility that trajectory errors might be contributing to the bias we find with the MOZAIC-IAGOS CO dataset, we have also compared MOZAIC-IAGOS in situ CO profiles against MOPITT retrievals. As an example in Fig. 8, we display the comparison between MOZAIC-IAGOS in situ CO profiles at Frankfurt (Germany) and MOPITT CO retrievals over Frankfurt from MOPITT overpasses. The MOZAIC-IAGOS in situ aircraft CO values have been transformed using the MOPITT averaging kernels and a priori data, for the period from December 2001–December 2012. MOPITT and MOZAIC-IAGOS are again strongly correlated, and biases at 500 and 300 hPa are large, and in fact very similar in magnitude to those with respect to the trajectory-mapped MOZAIC-IAGOS CO dataset.

A global comparison between the trajectory-mapped MOZAIC-IAGOS climatology and MOPITT at 600 hPa is displayed in Fig. 9. As can be seen from the same figure both datasets capture major features of the CO distribution, particularly anthropogenically polluted (i.e., northeast China) and biomass burning (i.e., west Africa, central Africa, South Africa and central America) regions. The CO-rich air in the lower troposphere over west Africa, where biomass burning fires are active, is convectively lifted vertically upward to the upper troposphere where it disperses over the African tropics towards the east coast of South America and the south Arabian peninsula (Edwards et al., 2003). In this region, higher CO VMRs are measured by MOZAIC-IAGOS than MOPITT. Over southeast Asia, MOZAIC-IAGOS detects highly polluted air-masses. In

ACPD
15, 29871–29937, 2015

these areas MOZAIC-IAGOS also measures higher CO than MOPITT. Comparison of the panels for DJF with those for SON of Fig. 9 also show that the NH CO VMRs are much higher during December–February than September–November (a result of the difference in OH, as noted above) and the latitude gradient in December–February is higher than in September–November. This is because in the SH the seasonal peak in CO occurs in September–November. This comparison also reveals a shift of the biomass burning from central Africa to South Africa and central America. Both datasets capture this, although the TIR/NIR product offers the greatest sensitivity to CO in the lower troposphere (Deeter et al., 2014). MOZAIC-IAGOS shows higher CO concentrations in these regions than MOPITT. On the other hand, Liu et al. (2005) suggested that since MOPITT (V3 L2) has low sensitivity to CO in the lower troposphere, the CO VMR estimated may only be a lower bound. The same authors noted that fires can be missed if not large enough or if they do not coincide with the MOPITT overpass time, or both. The presence of clouds is also another limitation for missing data.

Figure S2 shows global maps of percentage differences between MOPITT and the transformed trajectory-mapped MOZAIC-IAGOS CO climatology at 800 and 600 hPa pressure levels for DJF and SON 2001–2012. Differences are generally less than ±20 % at 800 hPa, with a negligible overall bias, but larger at 600 hPa, with MOPITT on average 10–20 % higher except few places over the Caribbean, southeast Asia and central Africa. Generally, the comparisons of the CO profiles of the transformed trajectory-mapped MOZAIC-IAGOS and MOPITT for both grid cells as well as zonal mean for different latitude bands show a consistent, significant bias: MOPITT is lower from about 700 to 300 hPa, but shows a negligible bias in the lowermost troposphere. Above 300 hPa, they seem to agree better, although this may be partly due to the fact that the retrieved CO values in this region are highly influenced by the MOPITT a priori data for both cases.

ACPD
15, 29871–29937, 2015

4.2 Comparison with MOPITT CO total column values

CO total column amounts are retrieved from the MOPITT observations in addition to the profile retrievals. The retrieved CO total column c_{ret} (a scalar) is related to the retrieved profile x_{ret} (a vector) through the linear relation

$$c_{\text{ret}} = \boldsymbol{t}^{\mathrm{T}} x_{\text{ret}} \tag{3}$$

where T indicates the transpose operation and $\boldsymbol{t}$ is the total column vectors. The CO total column averaging kernel can be calculated from the profile averaging kernels by

$$a = \boldsymbol{t}^{\mathrm{T}} \mathbf{A} \tag{4}$$

The column operator simply converts the mixing ratio for each retrieval level to a partial column amount. Using the hydrostatic relation, the operator $\boldsymbol{t}$ is expressed as

$$\boldsymbol{t} = 2.120 \times 10^{13} \Delta \boldsymbol{p} \tag{5}$$

Equation (5) is expressed in molecules $\mathrm{cm}^{-2}\,\mathrm{ppbv}^{-1}$ and $\Delta \boldsymbol{p}$ is the vector of the thicknesses of the retrieval pressure levels (in hPa). The interfaces of the retrieval layers are set at the surface, top of the atmosphere, and the midpoints between the standard nine retrieval levels. Determination of $\Delta \boldsymbol{p}$ required in Eq. (5) has to be made individually for each retrieval because of the variability of the surface pressure. The boundaries of the imaginary layer associated with each level are located at the pressure midpoints between the levels in the grid.

For example, for a surface pressure of 950 hPa, the fixed retrieval pressure grid levels along with surface pressure would be (950, 900, 800, 700, 600, 500, 400, 300, 200, 100) hPa. Hence the corresponding $\Delta \boldsymbol{p}$ values would be (25, 75, 100, 100, 100, 100, 100, 100, 100, 100) hPa. Column amounts are calculated from the in situ profiles according to Eq. (6) to validate the CO total column retrievals.

In the same manner as we have done for the retrieved CO profiles, the retrievals of CO total column c_{ret} may be compared against total column values derived from in situ

ACPD
15, 29871–29937, 2015

profiles x. Utilizing Eq. (2), the retrievals of the total CO column c_{ret} found in Eq. (3) can be rewritten alternatively as

$$c_{ret} = c_a + a(x - x_a) \quad (6)$$

where $c_a = \boldsymbol{t}^T x_a$ is the a priori total column value corresponding to the a priori profile x_a, a is the CO total column averaging kernel and x is the in situ profile.

We have calculated the global total CO columns for both the MOZAIC-IAGOS CO climatology (using the MOPITT a priori and averaging kernels by applying Eq. 6) and for MOPITT CO retrievals and compared different regions of the globe and different times from 2001–2012. The comparisons between the climatology and the MOPITT observations agree well, typically to within 10 %. For most regions the MOPITT CO total columns are slightly higher than the trajectory-mapped MOZAIC-IAGOS CO climatology total columns while in high CO source regions MOPITT seems to underestimate CO emissions. The SH shows a distinct latitude gradient, which not evident in the NH. This is likely related to the existence of major CO sources in the NH and the absence of large sources of emission in the SH. Nighttime CO observations of MOPITT have not been validated and appear subject to larger bias (Heald et al., 2004). Hence, we use the daytime data for comparison.

Figure 10 shows total column CO for August 2002, December 2005, December 2011 and August 2012. From Fig. 10, it is clear that MOPITT and the climatology are similarly able to capture the CO spatial variability. In August 2002 and 2012, elevated total column CO is seen over South America, southeast Asia and west African which is due primarily to agricultural biomass burning in the regions. In both months, we see high total column CO over southeast Asia and west Africa. High total column CO is also seen over eastern China, which is one of the major emission regions in the world. Northern hemispheric total columns are much higher than those in the Southern Hemisphere, and CO is somewhat more abundant in the NH winter (December), which is reasonable due to the lower amounts of hydroxyl radical (OH) that are present in the troposphere in that season (reduced oxidizing capacity). Generally, the MOPITT CO

ACPD
15, 29871–29937, 2015

total column retrievals are slightly higher than the trajectory-mapped MOZAIC-IAGOS CO climatology.

Figure S3 shows global difference plots for the CO maps shown Fig. 10. Biases generally lie within ±20 %, and the global mean bias between the MOPITT and MOZAIC-IAGOS CO climatology total columns is typically about 5 % or less. While overall bias shows MOPITT to be higher, it is also evident that the trajectory-mapped MOZAIC-IAGOS climatology is typically higher near major sources (eastern China, west central Africa and western South America) as well as over some areas of the oceans where aircraft data are not available. The negative biases near major sources are probably due to the limited vertical resolution of MOPITT as previously noted.

Similar results are found for other years (Fig. 11). This figure shows scatter plots of retrieved MOPITT CO total columns against the transformed trajectory-mapped MOZAIC-IAGOS climatology for August 2008, December 2008, August 2012 and December 2012. MOPITT and the trajectory-mapped climatology generally show strong correlations, and average biases of less than 5 %. MOPITT is higher most cases. This is consistent with previous work, which also shows positive total column retrieval bias against aircraft data (Deeter et al., 2014, 2013; Emmons et al., 2009, 2007).

5 Results

5.1 Global distribution of MOZAIC-IAGOS CO climatology

As an example, Fig. 12 shows the monthly mean CO VMR between 4 and 8 km altitude a.s.l. for the four seasons (i.e., December–February, March–May, June–August and September–November) during 2001–2012. The climatology is able to capture the CO spatial variability fairly well: the northern hemispheric concentrations are much higher, and the biomass burning peaks are clearly visible for the NH winter and spring seasons. The climatology shows more abundant CO in the NH during these seasons. This is due primarily to lower OH levels during the cold season which permits a longer

ACPD
15, 29871–29937, 2015

lifetime for CO, although there also appears to be an additional source in eastern Asia. Enhanced CO concentration is observed in the tropical regions where wildfire burning is typical during the December–February season, like west Africa and a large part of central Africa (Sauvage et al., 2005, 2007). At southern mid-latitudes between southern Africa and Australia, we observe high CO from September to November, during the agricultural burning season. This is accompanied by enhanced ozone in the same region (e.g. Ding et al., 2015; see also Sect. 5.2), produced via Reactions (R1)–(R5) and similar. Although Fig. 12 shows a 12-year global map, the strong enhanced CO over these regions (west Africa, South America, and southeast Asia) is clearly observable as an annual feature with significant interannual variability.

Furthermore, Fig. 12 allows us to examine the annual variation of the global distribution of CO between 4 and 8 km altitudes a.s.l. Despite the limited MOZAIC-IAGOS data in the SH, the seasonal cycle of CO is clearly shown in both hemispheres. The greatest change of CO from north to south occurs around the tropics in February–April when CO levels are greatest in the NH. The reverse gradient appears with a sharp decrease across the tropics in September–October when CO levels peak in the SH. High CO levels are seen in August between southeast Africa and southwest Australia, which is as a result of the long-range transport of CO produced from biomass burning in the tropical areas (i.e., southern Africa).

5.2 Zonal distribution of MOZAIC-IAGOS CO climatology

5.2.1 Seasonal variation

In Fig. 13, data are grouped in three bands representing the NH extratropics (Fig. 13c), the SH extratropics (Fig. 13d), the tropics (Fig. 13b) and for latitude band 45° S–45° N (Fig. 13a). The zonal mean trajectory-mapped MOZAIC-IAGOS CO climatology for these latitude bands is shown for the altitude ranges 0–2, 2–4, 4–8 and 8–12 km.

As can be seen from Fig. 13, CO shows distinct seasonal cycles in both hemispheres. In the NH extratropics (Fig. 13c), maximum CO VMR is observed in February–

ACPD
15, 29871–29937, 2015

April following a steady increase during fall and winter. This is followed by a rapid decrease giving rise to the lowest CO levels in July–August. The seasonal decline of CO VMR in summer shows the typical seasonal pattern of CO in the NH driven by OH increase during this time (Yurganov et al., 2008; Novelli et al., 1998). In the SH extratropics (Fig. 13d), CO levels peak in September–October. This is consistent with previous studies by Novelli et al. (1998). In the SH, the annual CO maximum is earlier at lower altitudes. Rinsland et al. (2002) suggested this phenomenon to be associated with the vertical and horizontal CO dispersion away from the biomass burning region in the tropics. Moreover, CO shows greater seasonal variability, particularly at higher altitudes, in the SH than in the NH. This can also be seen in Fig. 12. The seasonal CO cycle in the tropics (Fig. 13b) and for latitude band 45° S–45° N (Fig. 13a) both display a July minimum, and a secondary maximum in October while the primary maximum is in late NH winter/early spring. This CO cycle in both hemispheres is controlled by seasonal variations of OH, as OH is the major CO sink (Logan et al., 1981; Bergamaschi et al., 2000; Novelli et al., 1998) and the space–time distribution of its sources (Novelli et al., 1998), in particular the biomass burning either in the Tropics (largest fires occur in austral Africa and South America in SON) or at boreal latitudes (largest fires in June–July–August), and anthropogenic sources at northern mid-latitudes.

Figure 14 shows zonal mean latitude-time cross-section plots of CO VMR at 2.5, 4.5, 6.5, 8.5, 10.5 and 12.5 km altitudes for the period 2001–2012. The latitude-time cross-section shows the seasonal cycle of zonal mean CO for different altitudes, as seen in the previous figures, and also the variation of the interhemispheric CO VMR gradient throughout the year. The strongest interhemispheric gradient occurs in March, at low altitude, and the smallest gradients are seen in northern summer. The gradient in NH spring reverses at higher altitudes, and in NH fall where it is especially strong at higher altitudes. Plots 14e, f also clearly show the weak seasonal cycle in the NH upper troposphere compared to that in the SH.

ACPD
15, 29871–29937, 2015

5.2.2 Vertical distribution

Figure 15 illustrates the variation of CO with altitude for the seasons in which we observe maximum CO levels in both the SH and NH (i.e., MAM and SON). The seasons demonstrate the greatest CO VMRs at lower altitude in both hemispheres. Even though CO declines with altitude in both hemispheres, it does so faster in the NH than the SH, which results in a decrease in the strength of the interhemispheric gradient (SH to NH) with altitude. This result is consistent with Edwards et al. (2006) who suggested that in the absence of continued CO input from the source regions (i.e., biomass burning in southern Africa and South America), the aged CO is gradually distributed vertically throughout the troposphere in the SH. In fact, in regions where there is deep convection this leads to an enhanced CO concentration in the upper troposphere, as can be seen on the right-hand side of Fig. 15 and in Fig. 16d. Moreover, Liu et al. (2006) showed large horizontal CO gradients in association with vertical and horizontal transport of air originated from different chemical signatures.

The zonal CO mean vertical profiles for February, April, July and September, averaged for 2001–2012, are shown in Fig. 16. The results are displayed for latitude bands 23.5–66.5° N (NH extratropics), 23.5–66.5° S (SH extratropics) and 23.5° S-23.5° N (tropics). The CO profiles show strong seasonal and latitudinal variability. The largest VMRs of CO occur at lower altitudes in the NH extratropics in February and April but the strong decline with altitude causes CO VMRs to be higher in the SH at high altitudes than in the NH. In the SH in February, April, July and September, there is little variation of CO with altitude. This is due to the sampling of the lower most stratosphere in the NH much more frequently than in the SH. The trajectory-mapped CO in the SH extratropics is mainly representative of the tropics unlike in the NH extratropics where there are many CO measurements north of 40° N. The altitude gradients are similar in July and September, with CO levels in September in the SH higher than those in the NH. This is typically the influence of tropical biomass burning in South America and austral Africa, which are the two regions most represented in the climatology in the

ACPD
15, 29871–29937, 2015

SH. In tropics, CO VMRs show rapid decrease with altitude in the lower troposphere but above approximately 4–5 km changes with altitude are minor.

6 Applications

6.1 Global variation and trends of CO

The smoothed time series of the NH extratropical zonal mean CO VMR at 900, 700, 500, and 300 hPa for the trajectory-mapped MOZAIC-IAGOS dataset 2001–2012 is shown in Fig. 17. For purposes of comparison we also show data from MOPITT and from the mapped MOZAIC-IAGOS dataset transformed with the MOPITT averaging kernals. Gaps in the figure occur whenever one data source is missing. The gaps in June–July 2001 and August–September 2009 were due to a cooler failure of the MOPITT instrument. MOZAIC-IAGOS began CO measurement in December 2001 and there were only partial data available in 2010 and 2011. The observations show an annual late winter or springtime peak in the NH extratropical zonal CO loading each year, in conjunction with low wintertime OH levels. The same interannual cycle of CO is captured by both trajectory-mapped MOZAIC-IAGOS (transformed and untransformed) and MOPITT. They appear to track short-term changes equally well. However, while all show a modest decline in the lower troposphere particularity until about 2008–2009 (and then CO VMR seems to level off), in accordance with the trends found by Worden et al. (2013), in the upper troposphere MOPITT shows a modest increase, and a significant bias with respect to trajectory-mapped MOZAIC-IAGOS that decreases with time. Although the untransformed trajectory-mapped MOZAIC-IAGOS CO values show a significant difference against the transformed at lower troposphere, they seem to agree well at higher levels. However, the untransformed trajectory-mapped MOZAIC-IAGOS shows higher CO levels compared to MOPITT CO retrievals for all levels.

Laken and Shahbaz (2014) found increasing CO trends over widespread regions of South America, Mexico, central Africa, Greenland, the eastern Antarctic, and the entire

ACPD
15, 29871–29937, 2015

region of India and China from MOPITT data. Figure S4 shows similar time series for the SH extratropics, but the negative trend is not as clear as that in the NH due to limited data. The annual springtime peak in the SH zonal CO loading is again in all of the time series. This is predominantly associated with dry season biomass burning emissions in South America, southern Africa, southeast Asia, and northwestern Australia. In later months, the CO resulting from these emissions is generally destroyed by more active photochemistry during the SH summer. At these times, the retrieved zonal CO falls to background levels (around 40–50 ppbv) which are representative of the remote ocean regions where CO production by methane oxidation is the dominant source (Edwards et al., 2006). Biases between MOPITT and MOZAIC-IAGOS are again significant at all levels, but lowest in the lower troposphere, and again decrease with time. The untransformed trajectory-mapped MOZAIC-IAGOS data again show higher CO levels than the transformed CO climatology at all levels.

In Fig. S5, we display the time series of the zonal monthly mean of CO VMR for the tropics. The biases between the MOPITT retrievals and the trajectory-mapped MOZAIC-IAGOS in general show the same feature as the extratropics both in time and vertical levels. The CO values show seasonal patterns that combine the seasonal patterns of the NH and SH seen in Figs. 17 and S4.

In Sect. 4, we found significant biases between the MOPITT retrievals and the trajectory-mapped MOZAIC-IAGOS CO dataset. In Fig. S6, we display the monthly mean time series for Frankfurt from December 2001–December 2012. As can be seen from the figure, we notice again significant biases between MOPITT and the transformed MOZAIC-IAGOS in situ above 700 hPa, in good agreement with the result shown in Fig. 17. The biases also appear to decrease similarly with time in the upper troposphere. Furthermore, MOPITT shows a modest increase in CO levels in the upper troposphere while MOZAIC-IAGOS in situ (transformed and untransformed) shows a modest decline, consistent with Petetin et al. (2015) who report a similar decrease over Frankfurt. The MOPITT retrievals and MOZAIC-IAGOS (transformed and untransformed) CO values also show the same seasonal patterns as the NH extrat-

ACPD
15, 29871–29937, 2015

ropics (Fig. 17). This comparison indicates that a prominent bias, declining with time, exists between MOZAIC-IAGOS and MOPITT L3 V6 TIR/NIR products.

6.2 Global distribution of O_3–CO correlations

Global O_3 datasets have been developed by trajectory mapping of ozonesonde, aircraft and satellite measurements and validated (Tarasick et al., 2010; G. Liu et al., 2013; J. Liu et al., 2013; Osman et al., 2015). The maps show consistent agreement with independent in situ and satellite instruments. As a potential application of such datasets (O_3 and CO maps), we present here the relationship between O_3 and CO. The O_3–CO correlations were derived from the concurrent measurements of O_3 and CO using MOZAIC-IAGOS.

Since CO is involved in the production and destruction of O_3, studies of O_3–CO correlation can offer significant insight into the photochemical origin of air masses (e.g. Parrish et al., 1993; Chin et al., 1994; Zhang et al., 2008; Voulgarakis et al., 2011; Kim et al., 2013). A positive correlation is expected in regions where CO and O_3 are related due to emissions and photochemistry (for example, downwind of major CO and NO_x source regions and in the presence of a significant actinic flux). However, during winter, Parrish (1993) observed that O_3–CO were negatively correlated, presumably due to titration of O_3 by NO. Strong anticorrelation is also expected where stratospheric intrusions are a significant source of O_3, since CO mixing ratios in the stratosphere are quite low. For a remote maritime site, O_3–CO correlation would only be expected during periods when the site was downwind of significant CO and NO_x sources.

Although a quantitative interpretation in terms of O_3 production is complicated by sampling of air masses with varying background mixing ratios (Chin et al., 1994; Mauzerall et al., 1998), the correlation still provides valuable information about anthropogenic influence on O_3. Figures 19–21 examine the O_3–CO correlations observed by concurrent O_3 and CO measurements using MOZAIC-IAGOS instruments during the period from 2001–2012.

ACPD
15, 29871–29937, 2015

Figure 18 shows the global spatial distribution of O_3 and CO from the trajectory-mapped MOZAIC-IAGOS climatologies for June–August and September–November of 2001–2012 at 4.5 km a.s.l. The right panels of Fig. 18 show significantly enhanced CO and O_3 VMRs in the SH between southern Africa and Australia. In central Africa, where there is strong production of CO as a result of high biomass burning, there appears to be high O_3 concentrations during September–November in anthropogenically polluted and biomass burning regions. In the polluted region of east China O_3 is highest in the summer when photochemical activity is at its peak. The highest values of O_3 in the summertime are seen over the Middle East, north Africa and central Asia. The global spatial distribution of O_3 and CO from MOZAIC-IAGOS is generally consistent with previous OMI/AIRS results reported by Kim et al. (2013).

Correlation coefficients of the trajectory-mapped MOZAIC-IAGOS O_3 and CO climatology seasonal fields from 2001–2012 are displayed in Fig. 19. The seasonal O_3–CO correlations for the three-month time series (DJF, MAM, JJA, SON) of the O_3 and CO mixing ratios were computed for each grid. Figure 19 shows that in June–August and September–November, the O_3–CO correlation coefficients in the SH appear to be very strong positive in the southern midlatitudes in winter–spring. This suggests that in the SH winter, spring (and perhaps even in autumn) photochemical O_3 production is more dominant. In general, in the NH the O_3–CO correlations seem to be fairly positive in all seasons except the scattered low negative correlation coefficients seen in the spring (and perhaps even in autumn). This indicates that photochemical O_3 production clearly dominates most of the year at lower altitudes.

Figure 20 shows the O_3–CO correlation coefficients at 8.5 km altitude. In the SH strongly positive O_3–CO correlation coefficients are notable in all seasons except December–February, which suggests that photochemical O_3 production is dominant here even at this altitude. Strong negative correlations in the NH mid and higher latitudes in December–February and March–May indicate that the stratosphere is a major O_3 source at this altitude. In the NH summer where photochemical O_3 formation is a dominate source of O_3, positive O_3–CO correlation coefficients are seen, consistent

ACPD
15, 29871–29937, 2015

with previous work by Zahn et al. (2002). Moreover, the same figure shows (see also Fig. 21) that in all four seasons O_3–CO correlation coefficients in the tropics are positive. This is consistent with model calculations that estimate the O_3 abundance in the tropical upper troposphere originating from the stratosphere to be only 5–15 % (Roelofs and Lelieveld, 1997; Lamarque et al., 1999). Some fraction of the extratropical CO may originate as CO transported from tropical biomass-burning regions to the extratropics; however Bowman (2006) showed using MOPITT CO data that transport from the tropics to the extratropics is a comparatively slow process while the zonal dispersion of air parcels within the tropics and subtropics is relatively rapid.

As a summary, in Fig. 21 we display the distribution of the zonal mean of the O_3–CO correlation coefficients from the trajectory-mapped CO and O_3 datasets as a function of latitude and altitude for the period from 2001–2012. The figure shows that in the lower troposphere the O_3–CO correlations have generally positive values as photochemistry is the dominant source of O_3, and the stratospheric influence is relatively small. In the mid and upper troposphere, the influence of the influx of stratospheric air depends strongly on latitude and season, but it always affects calculated O_3–CO correlation coefficients. The NH high latitudes show negative correlations in winter, spring and fall, in agreement with previous studies (e.g. Voulgarakis et al., 2011; Parrish et al., 1998). Due to lack of sunlight, these regions do not experience intense photochemistry and are dominated by O_3 destruction or dry deposition or both (Voulgarakis et al., 2011). Even though stratospheric intrusion can drive the negative correlations in the region, it is more frequent in spring (Zhang et al., 2008). In the SH, strong correlations are seen at all altitudes in all seasons except December–February, in agreement with those reported by Kim et al. (2013).

Further division of the climatology into annual averages may provide a global view of CO changes and transport. As CO is involved in both the production and destruction of O_3, O_3–CO correlations derived from the trajectory-mapped MOZAIC-IAGOS CO and O_3 climatology datasets presented here may provide important insights into the origin of air masses and the budgets of O_3 and CO in the troposphere. Figure 21 demon-

ACPD
15, 29871–29937, 2015

strates one aspect of the value of the MOZAIC-IAGOS continuous, long-term, global, vertically resolved in situ measurements. Such routine commercial aircraft observations provide valuable information on atmospheric composition that can improve our understanding of global and regional air quality and the potential impact of greenhouse gases on climate change.

7 Conclusions

We have presented a three-dimensional (i.e., latitude, longitude, altitude) gridded climatology of CO developed by trajectory mapping of global MOZAIC-IAGOS data. This quasi-global climatology dataset offers a complement to global satellite measurements, at significantly higher vertical resolution, that facilitates visualization and comparison of different years and seasons, and offers insight into the global variation and trends of CO. Even though the MOZAIC-IAGOS aircraft data are unevenly distributed both in time and space across the globe, the trajectory-mapped dataset is uniformly distributed on a $5^{\circ} \times 5^{\circ} \times 1$ km grid. The trajectory-based interpolation method confers significant advantages over linear or quadratic interpolation. Major regional features of the global CO distribution are clearly evident in the CO maps for different seasons and altitudes. The trajectory-mapped CO shows distinct seasonal cycles with the CO annual maximum occurring in September–October in the SH, coincident with the tropical biomass burning season (Rinsland et al., 2002), and in April in the NH, while the tropics show distinct maxima in January–February and in October. The interhemispheric CO gradient is strongest in late winter/early spring, and smallest in northern summer. Time series analysis of the climatology shows that in the NH and the tropics CO is declining with time. This is consistent with the previous studies using ground-based, aircraft and satellite data, such as Petetin et al. (2015), Worden et al. (2013), Laken and Shahbaz (2014) and Novelli et al. (1998). (In the SH, due to limited MOZAIC-IAGOS data, a clear CO trend cannot be seen.) The consistency of our findings with those from other global datasets lends increased confidence that the CO climatology derived from trajectory

ACPD
15, 29871–29937, 2015

mapping of global MOZAIC-IAGOS data can be used for CO trend studies at regional and global scales.

The trajectory-mapped CO dataset has been validated by comparing maps constructed using only forward trajectories and using only backward trajectories. The two methods show similar global CO distribution patterns. Differences are most commonly 10 % or less, and found to be less than 30 % for almost all cases. They are typically less than 10 % at northern mid-latitudes and less than 20 % in the tropics between ±30° latitude, except in the Pacific and Atlantic oceans where it can reach as large as 30 %. The dataset has also been validated by comparison against in-situ MOZAIC-IAGOS aircraft measurements, where the data from the validation site are excluded from the trajectory-mapped data. Although the comparison shows larger differences below 2 km, the profiles from the two methods agree very well between 2 and 10 km with the magnitude of bias within 20 %. Furthermore, comparison between the trajectory-mapped and MOZAIC-IAGOS in situ CO cruise data shows that major regional features of the global CO distribution for different seasons are clearly evident in both maps and they agree very well qualitatively. This suggests that the trajectory-mapped CO data performs well not only near airports but also in remote areas.

The trajectory-mapped CO dataset has also been extensively compared with MOPITT retrievals. Between 700 and 300 hPa, a prominent bias, declining with time, exists between MOZAIC-IAGOS and MOPITT L3 V6 TIR/NIR products.

A small positive bias for CO total column is found, consistent with those previously reported for MOPITT (Deeter et al., 2014, 2013; Emmons et al., 2009, 2007).

Comparison of similar maps made using the concurrent O_3 measurements by MOZAIC-IAGOS permits some insight into the sources of tropospheric O_3. The O_3–CO correlation shows a significant seasonal and latitudinal variation. In the tropics, where the influence by stratospheric air is small, generally positive correlations are seen, as photochemistry is the dominant source of O_3. In the extratropics, strong negative correlations in the NH winter, spring and autumn indicate that the influx of stratospheric air is a primary source, especially in the upper troposphere, while the picture is mixed

ACPD
15, 29871–29937, 2015

in the summer. Strong O_3–CO correlations are noted in all seasons except December–February over southern Africa, which suggests that photochemistry is generally the predominant O_3 source in this region.

Such constraints on tropospheric ozone sources can be useful for chemical transport model evaluation, as demonstrated by Kim et al. (2013). This unique 3-D CO climatology dataset will also be useful as model initial fields, and background and boundary fields. It will be especially useful as an improved a priori climatology for satellite data retrieval. The global picture it presents is also expected to be valuable for comparison and validation of model results.

The Supplement related to this article is available online at doi:10.5194/acpd-15-29871-2015-supplement.

Acknowledgements. The authors acknowledge the strong support of the European Commission, Airbus, and the Airlines (Lufthansa, Air-France, Austrian, Air Namibia, Cathay Pacific, Iberia and China Airlines so far) who carry the MOZAIC or IAGOS equipment and perform the maintenance since 1994. MOZAIC is presently funded by INSU-CNRS (France), Météo-France, Université Paul Sabatier (Toulouse, France) and Research Center Jülich (FZJ, Jülich, Germany). IAGOS has been additionally funded by the EU projects IAGOS-DS and IAGOS-ERI. The MOZAIC-IAGOS database is supported by ETHER (CNES and INSU-CNRS). Data are also available via Ether web site http://www.pole-ether.fr. We thank the many whose dedication makes such a dataset possible. The MOPITT team is appreciated for their datasets for validation. We acknowledge the trajectory model HYSPLIT (Hybrid Single Particle Lagrangian Integrated Trajectory Model) from the NOAA Air Resources Laboratory (http://www.arl.noaa.gov/ready.html), driven by the NCEP/NCAR reanalysis data from the NOAA/OAR/ESRL PSD, Boulder, Colorado, USA, at http://www.esrl.noaa.gov/psd/. The first author is grateful to the Natural Sciences and Engineering Research Council of Canada (NSERC) and Environment Canada for a research fellowship.

ACPD
15, 29871–29937, 2015

References

Bergamaschi, P., Hein, R., Heimann, M., and Crutzen, P. J.: Inverse modeling of the global CO cycle: 1. Inversion of CO mixing ratios, J. Geophys. Res., 105, 1909, doi:10.1029/1999JD900818, 2000.

Boden, T. A., Marland, G., and Andres, R. J.: Global, Regional, and National Fossil-Fuel CO_2 Emissions, Carbon Dioxide Information Analysis Center, Oak Ridge Natl. Lab., U.S. Dep. of Energy, Oak Ridge, Tenn., doi:10.3334/CDIAC/00001, available at: http://cdiac.ornl.gov/trends/emis/cpa.html (last access: 8 September 2015), 2009.

Bowman, K. W., Rodgers, C. D., Kulawik, S. S., Worden, J., Sarkissian, E., Osterman, G., Steck, T., Lou, M., Eldering, A., Shephard, M., Worden, H., Lampel, M., Clough, S., Brown, P., Rinsland, C., Gunson, M., and Beer, R.: Tropospheric emission spectrometer: retrieval method and error analysis, IEEE T. Geosci. Remote, 44, 1297–1307, 2006.

Brook, J. R., Dann, T. F., Galarneau, E., Herod, D., and Charland, J.-P.: The state of air quality in Canada: national patterns, in: Air Quality Management, Canadian Perspectives on a Global Issue, Springer, Dordrecht, ISBN 978-94-007-7557-2, 43–67, doi:10.1007/978-94-007-7557-2, 2014.

Cai, H. and Xie, S.: Estimation of vehicular emission inventories in China from 1980 to 2005, Atmos. Environ., 44, 8963–8979, 2007.

Carmichael, G. R., Tang, Y., Kurata, G., Uno, I., Streets, D. G., Woo, J.-H., Huang, H., Yienger, J., Lefer, B., Shetter, R. E., Blake, D. R., Atlas, E., Fried, A., Apel, E., Eisele, F., Cantrell, C., Avery, M. A., Barrick, J. D., Sachse, G. W., Brune, W. L., Sandholm, S. T., Kondo, Y., Singh, H. B., Talbot, R. W., Bandy, A., Thorton, D., Clarke, A. D., and Heikes, B. G.: Regional-scale chemical transport modeling in support of intensive field experiments: overview and analysis of the TRACE-P observations, J. Geophys. Res., 108, 8823, doi:10.1029/2002JD003117, 2003.

Chameides, W. L., Kasibhatla, P. S., Yienger, J. J., Levy II, H., and Moxim, W. J.: The growth of continental-scale metro-agro-plexes, regional ozone pollution, and world food production, Science, 264, 74–77, 1994.

Chin, M., Jacob, D. J., Munger, J. W., Parrish, D. D., and Doddridge, B. G.: Relationship of ozone and carbon monoxide over North America, J. Geophys. Res., 99, 14565–14573, 1994.

Clark, H., Sauvage, B., Thouret, V., Nédélec, P., Blot, R., Wang, K. Y., Smit, H., Neis, P., Petzold, A., Athier, G., Boulanger, D., Cousin, J.-M., Beswick, K., Gallagher, M., Baumgard-

ACPD
15, 29871–29937, 2015

ner, D., Kaiser, J., Flaud, J.-M., Wahner, A., Volz-Thomas, A., and Cammas, J.-P.: The first regular measurements of ozone, carbon monoxide and water vapour in the Pacific UTLS by IAGOS, Tellus B, 67, 28385, doi:10.3402/tellusb.v67.28385, 2015.

Crutzen, P. A.: A discussion of the chemistry of some minor constituents in the stratosphere and troposphere, Pure Appl. Geophys., 106–108, 1385–1399, 1973.

Deeter, M. N., Emmons, L. K., Edwards, D. P., Gille, J. C., and Drummond, J. R.: Vertical resolution and information content of CO profiles retrieved by MOPITT, Geophys. Res. Lett., 31, L15112, doi:10.1029/2004GL020235, 2004.

Deeter, M. N., Martínez-Alonso, S., Edwards, D. P., Emmons, L. K., Gille, J. C., Worden, H. M., Pittman, J. V., Daube, B. C., and Wofsy, S. C.: Validation of MOPITT Version 5 thermal-infrared, near-infrared, and multispectral carbon monoxide profile retrievals for 2000–2011, J. Geophys. Res., 118, 6710–6725, doi:10.1002/jgrd.50272, 2013.

Deeter, M. N., Martínez-Alonso, S., Edwards, D. P., Emmons, L. K., Gille, J. C., Worden, H. M., Sweeney, C., Pittman, J. V., Daube, B. C., and Wofsy, S. C.: The MOPITT Version 6 product: algorithm enhancements and validation, Atmos. Meas. Tech., 7, 3623–3632, doi:10.5194/amt-7-3623-2014, 2014.

Ding, K., Liu, J., Ding, A., Liu, Q., Zhao, T. L., Shi, J., Han, Y., Wang, H., and Jiang, F.: Uplifting of carbon monoxide from biomass burning and anthropogenic sources to the free troposphere in East Asia, Atmos. Chem. Phys., 15, 2843–2866, doi:10.5194/acp-15-2843-2015, 2015.

Draxler, R. R.: HYSPLIT4 User's Guide, NOAA Tech. Memo, ERL ARL-230, NOAA Air Resourcesn Laboratory, Silver Spring, MD, 1999.

Draxler, R. R. and Hess, G. D.: An overview of the Hysplit_4 modeling system for trajectories, dispersion, and deposition, Aust. Meteorol. Mag., 47, 295–308, 1998.

Drummond, J. R. and Mand, G. S.: The Measurements of Pollution in the Troposphere (MOPITT) instrument: overall performance and calibration requirements, J. Atmos. Ocean. Tech., 13, 314–320, 1996.

Edwards, D. P., Halvorson, C., and Gille, J. C.: Radiative transfer modeling of the EOS Terra Satellite Measurements of Pollution in the Troposphere (MOPITT) instrument, J. Geophys. Res., 104, 16755–16775, 1999.

Edwards, D. P., Lamarque, J.-F., Attie', J.-L., Emmons, L. K., Richter, A., Cammas, J.-P., Gille, J. C., Francis, G. L., Deeter, M. N., Warner, J., Ziskin, D. C., Lyjak, L. V., Drummond, J. R., and Burrows., J. P.: Tropospheric ozone over the tropical Atlantic: a satellite perspective, J. Geophys. Res., 108, 4237, doi:10.1029/2002JD002927, 2003.

ACPD
15, 29871–29937, 2015

Edwards, D. P., Petron, G., Novelli, P. C., Emmons, L. K., Gille, J. C., and Drummond, J. R.: Southern Hemisphere carbon monoxide interannual variability observed by Terra/Measurement of Pollution in the Troposphere (MOPITT), J. Geophys. Res., 111, D16303, doi:10.1029/2006JD007079, 2006.

Emmons, L. K., Gille, J. C., Edwards, D. P., Attie', J.-L, Warner, J., Ziskin, D., Francis, G., Khattatov, B., Yudin, V., Lamarque, J.-F., Ho, S.-P., Mao, D., Chen, J. S., Drummond, J., Novelli, P., Sachse, G., Coffey, M. T., Hannigan, J. W., Gerbig, C., Kawakami, S., Kondo, Y., Takegawa, N., Schlager, H., Baehr, J., and Ziereis, H.: Validation of Measurements of Pollution in the Troposphere (MOPITT) CO retrievals with aircraft in situ profiles, J. Geophys. Res., 109, D03309, doi:10.1029/2003JD004101, 2004.

Emmons, L. K., Pfister, G. G., Edwards, D. P., Gille, J. C., Sachse, G., Blake, D., Wofsy, S., Gerbig, C., Matross, D., and Nédélec, P.: Measurements of Pollution in the Troposphere (MOPITT) validation exercises during summer 2004 field campaigns over North America, J. Geophys. Res., 112, D12S02, doi:10.1029/2006JD007833, 2007.

Emmons, L. K., Edwards, D. P., Deeter, M. N., Gille, J. C., Campos, T., Nédélec, P., Novelli, P., and Sachse, G.: Measurements of Pollution In The Troposphere (MOPITT) validation through 2006, Atmos. Chem. Phys., 9, 1795–1803, doi:10.5194/acp-9-1795-2009, 2009.

Fishman, J. and Seiler, W.: Correlative nature of ozone and carbon monoxide in the troposphere: implications for the tropospheric ozone budget, J. Geophys. Res., 88, 3662–3670, 1983.

Galanter, M., Levy II, H., and Carmichael, G. R.: Impacts of biomass burning on tropospheric CO, NO_x, and Os, J. Geophys. Res., 105, 6633–6653, 2000.

Granier, C., Bessagnet, B., Bond, T., D'Angiola, A., v. d. Gon, H. D., Frost, G. J., Heil, A., Kaiser, J. W., Kinne, S., Klimont, Z., Kloster, S., Lamarque, J.-F., Liousse, C., Masui, T., Meleux, F., Mieville, A., Ohara, T., Raut, J.-C., Riahi, K., Schultz, M. G., Smith, S. J., Thomson, A., v. Aardenne, J., v. d. Werf, G. R., and v. Vuuren, D. P.: Evolution of anthropogenic and biomass burning emissions of air pollutants at global and regional scales during the 1980–2010 period, Climatic Change, 109, 163–190, doi:10.1007/s10584-011-0154-1, 2011.

Gregg, J. S., Andres, R. J., and Marland, G.: China: emissions pattern of the world leader in CO_2 emissions from fossil fuel consumption and cement production, Geophys. Res. Lett., 35, L08806, doi:10.1029/2007GL032887, 2008.

Heald, C. L., Jacob, D. J., Jones, D. B. A., Palmer, P. I., Logan, J. A., Streets, D. G., Sachse, G. W., Gille, J. C., Hoffman, R. N., and Nehrkorn, T.: Comparative inverse analy-

ACPD
15, 29871–29937, 2015

sis of satellite (MOPITT) and aircraft (TRACE-P) observations to estimate Asian sources of carbon monoxide, J. Geophys. Res., 109, D15S04, doi:10.1029/2004JD005185, 2004.
Holloway, T., Levy II, H., and Kasibhatla, P.: Global distribution of carbon monoxide, J. Geophys. Res., 105, 12123–12147, 2000.
Hoor, P., Gurk, C., Brunner, D., Hegglin, M. I., Wernli, H., and Fischer, H.: Seasonality and extent of extratropical TST derived from in-situ CO measurements during SPURT, Atmos. Chem. Phys., 4, 1427–1442, doi:10.5194/acp-4-1427-2004, 2004.
Hubler, G., Montzka, D. D., Norton, R. B., Murphy, P. C., Fehsenfeld, F. C., Liu, S. C., Ridley, B. A., Walega, J. G., Atlas, E., Grahek, F. E., Heidt, L. E., Merrill, J., Huebert, B. J., and Bodhaine, B. A.: Total reactive oxidized nitrogen (NO_y) in the remote pacific troposphere and its correlation with O3 and CO: Mauna Loa Observatory Photochemistry Experiment 1988, 25, J. Geophys. Res., 97, 10427–10447, 1992.
Jacob, D. J., Crawford, J. H., Kleb, M. M., Connors, V. S., Bendura, R. J., Raper, J. L., Sachse, G. W., Gille, J. C., Emmons, L., and Heald, C. L.: Transport and Chemical Evolution over the Pacific (TRACE-P) aircraft mission: design, execution, and first results, J. Geophys. Res., 108, 9000, doi:10.1029/2002JD003276, 2003.
Jaffe, D. A., Honrath, R. E., Zhang, L., Akimoto, H., Shimizu, A., Mukai, H., Murano, K., Hatakeyama, S., and Merrill, J.: Measurements of NO, NO_y, CO, and O_3 and estimation of the ozone production rate at Oki Island, Japan during PEM-West, J. Geophys. Res., 101, 2037–2048, 1996.
Kalnay, E., Kanamitsu, M., Kistler, R., Collins, W., Deaven, D., Gandin, L., Iredell, M., Saha, S., White, G., Woollen, J., Zhu, Y., Leetmaa, A., Reynolds, R., Chelliah, M., Ebisuzaki, W., Higgins, W., Janowiak, J., Mo, K. C., Ropelewski, C., Wang, J., Jenne, R., and Joseph, D.: The NCEP/NCAR 40-year reanalysis project, B. Am. Meteorol. Soc., 77, 437–471, 1996.
Khalil, M. A. K. and Rasmussen, R. A.: Carbon monoxide in the Earth's atmosphere: indications of a global increase, Nature, 332, 242–245, 1988.
Khalil, M. A. K. and Rasmussen, R. A.: Global decrease in atmospheric carbon monoxide concentration, Nature, 370, 639–641, 1994.
Kim, P. S., Jacob, D. J., Liu, X., Warner, J. X., Yang, K., Chance, K., Thouret, V., and Nedelec, P.: Global ozone–CO correlations from OMI and AIRS: constraints on tropospheric ozone sources, Atmos. Chem. Phys., 13, 9321–9335, doi:10.5194/acp-13-9321-2013, 2013.

ACPD
15, 29871–29937, 2015

Laken, B. and Shahbaz, T.: Satellite-detected carbon monoxide pollution during 2000–2012: examining global trends and also regional anthropogenic periods over China, the EU and the USA, Climate, 2, 1–16, doi:10.3390/cli2010001, 2014.
Lamarque, J.-F., Hess, P. G., and Tie, X. X.: Three-dimensional model study of the influence of stratosphere–troposphere exchange and its distribution on tropospheric chemistry, J. Geophys. Res., 104, 26363–26372, 1999
Law, K. S. and Pyle, J. A.: Modeling trace gas budgets in the troposphere, 2. CH_4 and CO, J. Geophys. Res., 98, 18401–18412, doi:10.1029/93JD01480, 1993.
Lelieveld, J., Crutzen, P. J., Ramanathan, V., Andreae, M. O., Brenninkmeijer, C. A. M., Campos, T., Cass, G. R., Dickerson, R. R., Fischer, H., de Gouw, J. A., Hansel, A., Jefferson, A., Kley, D., de Laat, A. T. J., Lal, S., Lawrence, M. G., Lobert, J. M., Mayol-Bracero, O. L., Mitra, A. P., Novakov, T., Oltmans, S. J., Prather, K. A., Reiner, T., Rodhe, H., Scheeren, H. A., Sikka, D., and Williams, J.: The Indian Ocean Experiment: widespread air pollution from South and Southeast Asia, Science, 291, 1031–1036, 2001.
Liu, G., Tarasick, D. W., Fioletov, V. E., Sioris, C. E., and Rochon, Y. J.: Ozone correlation lengths and measurement uncertainties from analysis of historical ozonesonde data in North America and Europe, J. Geophys. Res., 114, D04112, doi:10.1029/2008JD010576, 2009.
Liu, G., Liu, J., Tarasick, D. W., Fioletov, V. E., Jin, J. J., Moeini, O., Liu, X., Sioris, C. E., and Osman, M.: A global tropospheric ozone climatology from trajectory-mapped ozone soundings, Atmos. Chem. Phys., 13, 10659–10675, doi:10.5194/acp-13-10659-2013, 2013.
Liu, H., Jacob, D. J., Bey, I., Yantosca, R. M., Duncan, B. N., and Sachse, G. W.: Transport pathways for Asian combustion outflow over the Pacific: interannual and seasonal variations, J. Geophys. Res., 108, 8786, doi:10.1029/2002JD003102, 2003.
Liu, J., Drummond, J. R., Li, Q., Gille, J. C., and Ziskin, D. C.: Satellite mapping of CO emission from forest fires in Northwest America using MOPITT measurements, Remote Sens. Environ., 95, 502–516, 2005.
Liu, J., Drummond, J. R., Jones, D. B. A., Cao, Z., Bremer, H., Kar, J., Zou, J., Nichitiu, F., and Gille, J. C.: Large horizontal gradients in atmospheric CO at the synoptic scale as seen by spaceborne measurements of pollution in the troposphere, J. Geophys. Res., 111, D02306, doi:10.1029/2005JD006076, 2006.
Liu, J., Tarasick, D. W., Fioletov, V. E., McLinden, C., Zhao, T., Gong, S., Sioris, C., Jin, J. J., Liu, G., and Moeini, O.: A global ozone climatology from ozone soundings via trajectory mapping:

ACPD
15, 29871–29937, 2015

a stratospheric perspective, Atmos. Chem. Phys., 13, 11441–11464, doi:10.5194/acp-13-11441-2013, 2013.
Logan, J. A., Prather, M. J., Wofsy, S. C., and McElroy, M. B.: Tropospheric chemistry: a global perspective, J. Geophys. Res., 86, 7210–7254, 1981.
Luo, M., Rinsland, C. P., Rodgers, C. D., Logan, J. A., Worden, H., Kulawik, S., Eldering, A., Goldman, A., Shephard, M. W., Gunson, M., and Lampel, M.: Comparison of carbon monoxide measurements by TES and MOPITT: influence of a priori data and instrument characteristics on nadir atmospheric species retrievals, J. Geophys. Res., 112, D09303, doi:10.1029/2006JD007663, 2007.
Marenco, A., Thouret, V., Nedelec, P., Smit, H., Helten, M., Kley, D., Karcher, F., Simon, P., Law, K., Pyle, J., Poschmann, G., Wrede, R. V., Hume, C., and Cook, T.: Measurements of ozone and water vapour by Airbus in-service aircraft: the MOZAIC airborne program, an overview, J. Geophys. Res., 103, 25631–25642, 1998.
Mauzerall, D. L., Jacob, D. J., Fan, S.-M., Bradshaw, J. D., Gregory, G. L., Sachse, G. W., and Blake, D. R.: Origin of tropospheric ozone at remote high northern latitudes in summer, J. Geophys. Res., 101, 4175–4188, 1996.
Mauzerall, D. L., Logan, J. A., Jacob, D. J., Anderson, B. E., Blake, D. R., Bradshaw, J. D., Heikes, B., Sachse, G. W., and Singh, H., and Talbot, B.: Photochemistry in biomass burning plumes and implications for tropospheric ozone over the tropical South Atlantic, J. Geophys. Res., 103, 8401–8423, 1998.
Mauzerall, D. L., Narita, D., Akimoto, H., Horowitz, L., Walters, S., Hauglustaine, D. A., and Brasseur, G.: Seasonal characteristics of tropospheric ozone production and mixing ratios over East Asia: a global three dimensional chemical transport and model analysis, J. Geophys. Res., 105, 17895–17910, 2000.
McKee, D. J. (Ed.): Tropospheric Ozone: Human Health and Agricultural Impacts, Boca Raton, Fla.: Lewis Publishers, 39–208, 1993.
Nedelec, P., Cammas, J.-P., Thouret, V., Athier, G., Cousin, J.-M., Legrand, C., Abonnel, C., Lecoeur, F., Cayez, G., and Marizy, C.: An improved infrared carbon monoxide analyser for routine measurements aboard commercial Airbus aircraft: technical validation and first scientific results of the MOZAIC III programme, Atmos. Chem. Phys., 3, 1551–1564, doi:10.5194/acp-3-1551-2003, 2003.
Nédélec P., Thouret, V., Brioude, J., Sauvage, B., and Cammas, J.-P., and Sthol, A.: Extreme CO concentrations in the upper troposphere over North–East Asia in June 2003 from the

ACPD
15, 29871–29937, 2015

in-situ MOZAIC aircraft data, Geophys. Res. Lett., 32, L14807, doi:10.1029/2005GL023141, 2005.
Nédélec, P., Blot, R., Boulanger, D., Athier, G., Cousin, J.-M., Gautron, B., Petzold, A., Volz-Thomas, A., and Thouret, V.: Instrumentation on commercial aircraft for monitoring the atmospheric composition on a global scale: the IAGOS system, technical overview of ozone and carbon monoxide measurements, Tellus B, 67, 27791, doi:10.3402/tellusb.v67.2779, 2015.
Novelli, P. C., Masarie, K. A., Tans, P. P., and Lang, P. M.: Recent changes in atmospheric carbon monoxide, Science, 263, 1587–1590, 1994.
Novelli, P. C., Masarie, K. A., and Lang, P. M.: Distributions and recent changes of carbon monoxide in the lower troposphere, J. Geophys. Res., 103, 19015–19033, 1998.
Novelli, P. C., Masarie, K. A., Lang, P. M., Hall, B. D., Myers, R. C., and Elkins, J. W.: Reanalysis of tropospheric CO trends: effects of the 1997–1998 wildfires, J. Geophys. Res., 108, 4464, doi:10.1029/2002JD003031, 2003.
Osman, M., Tarasick, D. W., Liu, J., Thouret, V., Fioletov, V. E., Moeini, O., McLinden, C., Sioris, C., Parrington, M., and Nédélec, P.: Ozone climatology derived from the Trajectory Mapping of Global aircraft (MOZAIC-IAGOS), satellite (ACE-FTS, SAGE) and extended ozonesonde data, in preparation, 2015.
Pan, L. L., Konopka, P., and Browell, E. V.: Observations and model simulations of mixing near the extratropical tropopause, J. Geophys. Res., 111, D05106, doi:10.1029/2005JD006480, 2006.
Parrish, D. D.: Carbon monoxide and light alkanes at tropospheric tracers of anthropogenic ozone, in: The Tropospheric Chemistry of Ozone in the Polar Regions, edited by: Niki, H. and Becker, K. H., Springer-Verlag, Berlin, 155–169, 1993.
Parrish, D. D., Trainer, M., Buhr, M. P., Watkins, B. A., and Fehsenfeld, F. C.: Carbon monoxide concentrations and their relation to concentrations of total reactive oxidized nitrogen at two rural U.S. sites, J. Geophys. Res., 96, 9309–9320, 1991.
Parrish, D. D., Holloway, J. S., Trainer, M., Murphy, P. C., Forbes, G. L., and Fehsenfeld, F. C.: Export of North American ozone pollution to the North Atlantic Ocean, Science, 259, 1436–1439, 1993.
Parrish, D. D., Trainer, M., Holloway, J. S., Yee, J. E., Warshawsky, M. S., Fehsenfeld, F. C., Forbes, G. L., and Moody, J. L.: Relationships between ozone and carbon monoxide at surface sites in the North Atlantic region, J. Geophys. Res., 103, 13357–13376, 1998.

ACPD
15, 29871–29937, 2015

Petetin, H., Thouret, V., Fontaine, A., Sauvage, B., Athier, G., Blot, R., Boulanger, D., Cousin, J.-M., and Nedelec, P.: Characterizing tropospheric ozone and CO around Frankfurt between 1994–2012 based on MOZAIC-IAGOS aircraft measurements, Atmos. Chem. Phys. Discuss., 15, 23841–23891, doi:10.5194/acpd-15-23841-2015, 2015.

Petzold, A., Thouret, V., Gerbig, C., Zahn, A., Brenninkmeijer, C. A. M., Gallagher, M., Hermann, M., Pontaud, M., Ziereis, H., Boulanger, D., Marshall, J., Nédélec, P., Smit, H. G. J., Frieß, U., Flaud, J.-M., Wahner, A., Cammas, J.-P., Volz-Thomas, A., and IAGOS Team: Global-scale atmosphere monitoring by in-service aircraft – current achievements and future prospects of the European research infrastructure IAGOS, Tellus B, 67, doi:10.3402/tellusb.v67.28452, 2015.

Ploeger, F., Konopka, P., Günther, G., Grooß, J.-U., and Müller, R.: Impact of the vertical velocity scheme on modeling transport across the tropical tropopause layer, J. Geophys. Res., 115, D03301, doi:10.1029/2009JD012023, 2010.

Ploeger, F., Konopka, P., Müller, R., Günther, G., Grooß, J.-U., Schiller, C., Ravegnani, F., Ulanovski, A., and Riese, M.: Backtrajectory reconstruction of water vapour and ozone in-situ observations in the TTL, Meteorol. Z., 21, 239–244, 2012.

Pommrich, R., Müller, R., Grooß, J.-U., Konopka, P., Ploeger, F., Vogel, B., Tao, M., Hoppe, C. M., Günther, G., Spelten, N., Hoffmann, L., Pumphrey, H.-C., Viciani, S., D'Amato, F., Volk, C. M., Hoor, P., Schlager, H., and Riese, M.: Tropical troposphere to stratosphere transport of carbon monoxide and long-lived trace species in the Chemical Lagrangian Model of the Stratosphere (CLaMS), Geosci. Model Dev., 7, 2895–2916, doi:10.5194/gmd-7-2895-2014, 2014.

Reichle Jr., H. G., Connors, V. S., Holland, J. A., Sherrill, R. T., Wallio, H. A., Casas, J. C., Condon, E. P., Gormsen, B. B., and Seiler, W.: The distribution of middle tropospheric carbon monoxide during early October 1984, J. Geophys. Res., 95, 9845–9856, 1990.

Reichle Jr., H. G., Anderson,B. E., Connors, V. S., Denkins, T. C., Forbes, D. A., Gormsen, B. B., Langenfelds, R. L., Neil, D. O., Nolf, S. R., Novelli, P. C., Pougatchev, N. S., Roell, M. M., and Steele, L. P.: Space shuttle based global CO measurements during April and October 1994, MAPS instrument, data reduction, and data validation, J. Geophys. Res., 104, 21443–21454, 1999.

Rinsland, C. P. and Levine, J. S.: Free tropospheric carbon monoxide concentrations in 1950 and 1951 deduced from infrared total column amount measurements, Nature, 318, 250–254, 1985.

ACPD
15, 29871–29937, 2015

Rinsland, C. P., Jones, N. B., Connor, B. J., Wood, S. W., Goldman, A., Stephen, T. M., Murcray, F. J., Chiou, L. S., Zander, R., and Mahieu, E.: Multiyear infrared solar spectroscopic measurements of HCN, CO, C_2H_6, and C_2H_2 tropospheric columns above Lauder, New Zealand (45° S latitude), J. Geophys. Res., 107, 1–12, 2002.

Rodgers, C. D.: Inverse Methods for Atmospheric Sounding: Theory and Practice, World Sci., Hackensack, N.J., 2000.

Roelofs, G.-J. and Lelieveld, J.: Model study of the influence of cross tropopause O_3 transports on tropospheric O_3 levels, Tellus B, 49, 38–55, 1997.

Sauvage, B., Thouret, V., Cammas, J.-P., Gheusi, F., Athier, G., and Nédélec, P.: Tropospheric ozone over Equatorial Africa: regional aspects from the MOZAIC data, Atmos. Chem. Phys., 5, 311–335, doi:10.5194/acp-5-311-2005, 2005.

Sauvage, B., Gheusi, F., Thouret, V., Cammas, J.-P., Duron, J., Escobar, J., Mari, C., Mascart, P., and Pont, V.: Medium-range mid-tropospheric transport of ozone and precursors over Africa: two numerical case studies in dry and wet seasons, Atmos. Chem. Phys., 7, 5357–5370, doi:10.5194/acp-7-5357-2007, 2007.

Schoeberl, M. R., Douglass, A. R., Zhu, Z. X., and Pawson, S.: A comparison of the lower stratospheric age spectra derived from a general circulation model and two data assimilation systems, J. Geophys. Res., 108, 4113, doi:10.1029/2002JD002652, 2003.

Shindell, D. T., Faluvegi, G., Stevenson, D. S., Krol, M. C., Emmons, L. K., Lamarque, J.-F., Pétron, G., Dentener, F. J., Ellingsen, K., Schultz, M. G., Wild, O., Amann, M., Atherton, C. S., Bergmann, D. J., Bey, I., Butler, T., Cofala, J., Collins, W. J., Derwent, R. G., Doherty, R. M., Drevet, J., Eskes, H. J., Fiore, A. M., Gauss, M., Hauglustaine, D. A., Horowitz, L. W., Isaksen, I. S. A., Lawrence, M. G., Montanaro, V., Müller, J.-F., Pitari, G., Prather, M. J., Pyle, J. A., Rast, S., Rodriguez, J. M., Sanderson, M. G., Savage, N. H., Strahan, S. E., Sudo, K., Szopa, S., Unger, N., van Noije, T. P. C., and Zeng, G.: Multi-model simulations of carbon monoxide: comparison with observations and projected near-future changes. J. Geophys. Res., 111, D19306, doi:10.1029/2006JD007100, 2006.

Stein, O., Schultz, M. G., Bouarar, I., Clark, H., Huijnen, V., Gaudel, A., George, M., and Clerbaux, C.: On the wintertime low bias of Northern Hemisphere carbon monoxide found in global model simulations, Atmos. Chem. Phys., 14, 9295–9316, doi:10.5194/acp-14-9295-2014, 2014.

Stohl, A.: Computation, accuracy and applications of trajectories – review and bibliography, Atmos. Environ., 32, 947–966, 1998.

ACPD
15, 29871–29937, 2015

Stohl, A. and Seibert, P.: Accuracy of trajectories as determined from the conservation of meteorological tracers, Q. J. Roy. Meteor. Soc., 125, 1465–1484, 1998.
Stohl, A., James, P., Forster, C., and Spichtinger, N.: An extension of Measurement of Ozone and Water Vapour by Airbus-In-service aircraft (MOZAIC) ozone climatologies using trajectory statistics, J. Geophys. Res., 106, D21, 27757–27768, doi:10.1029/2001JD000749, 2001.
Tan, Q., Chameides, W. L., Streets, D.,Wang, T., Xu, J., Bergin, M., and Woo, J.: An evaluation of TRACE-P emission inventories from China using a regional model and chemical measurements, J. Geophys. Res., 109, D22305, doi:10.1029/2004JD005071, 2004.
Tarasick, D. W., Jin, J. J., Fioletov, V. E., Liu, G., Tompson, A. M., Oltmans, S. J., Liu, J., Sioris, C. E., Liu, X., Cooper, O. R., Dann, T., and Thouret, V.: High-resolution tropospheric ozone fields for INTEX and ARCTAS from IONS ozonesondes, J. Geophys. Res., 115, D20301, doi:10.1029/2009JD012918, 2010.
Thompson, A. M.: The oxidizing capacity of the Earth's atmosphere – probable past and future changes, Science, 256, 1157–1165, doi:10.1126/science.256.5060.1157, 1992.
Tie, X., Brasseur, G. P., Zhao, C., Granier, C., Massie, S., Qin, Y., Wang, P., Wang, G., Yang, P., and Richter, A.: Chemical characterization of air pollution in eastern China and the eastern United States, Atmos. Environ., 40, 2607–2625, 2006.
Vogel, B., Pan, L. L., Konopka, P., Günther, G., Müller, R., Hall, W., Campos, T., Pollack, I., Weinheimer, A., Wei, J., Atlas, E. L., and Bowman, K. P.: Transport pathways and signatures of mixing in the extratropical tropopause region derived from Lagrangian model simulations, J. Geophys. Res., 116, D05306, doi:10.1029/2010JD014876, 2011.
Volz-Thomas, A., Berg, M., Heil, T., Houben, N., Lerner, A., Petrick, W., Raak, D., and Pätz, H.-W.: Measurements of total odd nitrogen (NO_y) aboard MOZAIC in-service aircraft: instrument design, operation and performance, Atmos. Chem. Phys., 5, 583–595, doi:10.5194/acp-5-583-2005, 2005.
Voulgarakis, A., Telford, P. J., Aghedo, A. M., Braesicke, P., Faluvegi, G., Abraham, N. L., Bowman, K. W., Pyle, J. A., and Shindell, D. T.: Global multi-year O_3–CO correlation patterns from models and TES satellite observations, Atmos. Chem. Phys., 11, 5819–5838, doi:10.5194/acp-11-5819-2011, 2011.
Wang, T., Carroll, M. A., Alber, G. M., Owens, K. R., Duderstadt, K. A., Markevitch, A., Parrish, D., Holloway, J., Fehsenfeld, F. C., Forbes, G., and Ogren, J.: Ground-based measure-

ACPD
15, 29871–29937, 2015

ments of NO_x and total reactive oxidized Nitrogen (NO_y) at Sable Island, Nova Scotia during the NARE 1993 Summer Intensive, J. Geophys. Res., 101, 28991–29004, 1996.
Wang, T., Lam, K. S., Chan, L. Y., Carroll, M. A., and Lee, A. S. Y.: Trace gas measurements in coastal Hong Kong during the PEM-WEST (B), J. Geophys. Res., 102, 28575–28588, 1997.
Wang, Y. X., McElroy, M. B., Wang, T., and Palmer, P. I.: Asian emissions of CO and NO_x: constraints from aircraft and Chinese station data, J. Geophys. Res., 109, D24304, doi:10.1029/2004JD005250, 2004.
Worden, H. M., Deeter, M. N., Frankenberg, C., George, M., Nichitiu, F., Worden, J., Aben, I., Bowman, K. W., Clerbaux, C., Coheur, P. F., de Laat, A. T. J., Detweiler, R., Drummond, J. R., Edwards, D. P., Gille, J. C., Hurtmans, D., Luo, M., Martínez-Alonso, S., Massie, S., Pfister, G., and Warner, J. X.: Decadal record of satellite carbon monoxide observations, Atmos. Chem. Phys., 13, 837–850, doi:10.5194/acp-13-837-2013, 2013.
Yurganov, L. N., McMillan, W., Dzhola, A. V., Grechko, E. I., Jones, N. B., and van der Werf, G. R.: Global AIRS and MOPITT CO measurements: validation, comparison, and links to biomass burning variations and carbon cycle, J. Geophys. Res., 113, 1–14, 2008.
Zahn, A., Brenninkmeijer, C. A. M., Asman, W. A. H., Crutzen, P. J., Heinrich, G., Fischer, H., Cuijpers, J. W. M., and van Velthoven, P. F. J.: Budgets of O3 and CO in the upper troposphere: CARIBIC passenger aircraft results 1997–2001, J. Geophys. Res., 107, 4337, doi:10.1029/2001JD001529, 2002.
Zander, R., Demoulin, P., Ehhalt, D. H., Schmidt, U., and Rinsland, C. P.: Secular increase of the total vertical column abundance of carbon monoxide above central Europe since 1950, J. Geophys. Res., 94, 11021–11028, 1989.
Zeng, G., Wood, S. W., Morgenstern, O., Jones, N. B., Robinson, J., and Smale, D.: Trends and variations in CO, C_2H_6, and HCN in the Southern Hemisphere point to the declining anthropogenic emissions of CO and C_2H_6, Atmos. Chem. Phys., 12, 7543–7555, doi:10.5194/acp-12-7543-2012, 2012.
Zhang, L., Jacob, D. J., Boersma, K. F., Jaffe, D. A., Olson, J. R., Bowman, K. W., Worden, J. R., Thompson, A. M., Avery, M. A., Cohen, R. C., Dibb, J. E., Flock, F. M., Fuelberg, H. E., Huey, L. G., McMillan, W. W., Singh, H. B., and Weinheimer, A. J.: Transpacific transport of ozone pollution and the effect of recent Asian emission increases on air quality in North America: an integrated analysis using satellite, aircraft, ozonesonde, and surface observations, Atmos. Chem. Phys., 8, 6117–6136, doi:10.5194/acp-8-6117-2008, 2008.

ACPD
15, 29871–29937, 2015

Zhang, L., Jacob, D. J., Liu, X., Logan, J. A., Chance, K., Eldering, A., and Bojkov, B. R.: Intercomparison methods for satellite measurements of atmospheric composition: application to tropospheric ozone from TES and OMI, Atmos. Chem. Phys., 10, 4725–4739, doi:10.5194/acp-10-4725-2010, 2010.

ACPD
15, 29871–29937, 2015

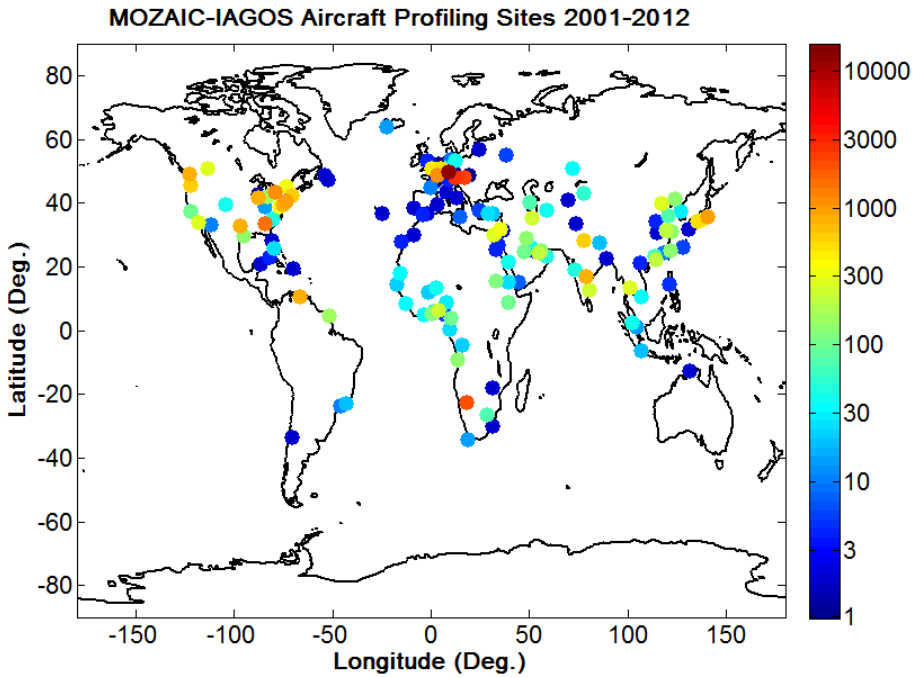

Figure 1. Airports stations visited by MOZAIC-IAGOS aircraft from 2001–2012. The color bar indicates the number of profiles available from each airport.

ACPD
15, 29871–29937, 2015

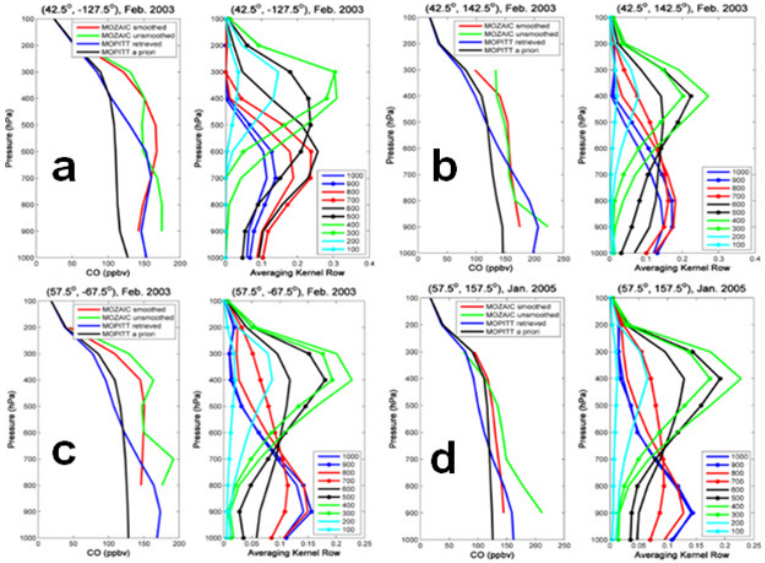

Figure 2. Examples of comparisons of monthly mean of the trajectory-mapped MOZAIC-IAGOS CO profiles, with the corresponding MOPITT's averaging kernels, a priori and retrievals. The left panels of each subplot show the original trajectory-mapped MOZAIC-IAGOS climatology profile (green, i.e. unsmoothed in the caption), the a priori profile (black), the transformed trajectory-mapped MOZAIC-IAGOS climatology profile (red, i.e. smoothed in the caption), and the MOPITT retrieved CO profile (blue). The right panels of each subplot show the mean averaging kernels obtained by averaging all daytime averaging kernels in the $5^\circ \times 5^\circ$ latitude–longitude box centered on the coordinates indicated. The different colors of the averaging kernel curves indicate the different pressure levels.

ACPD
15, 29871–29937, 2015

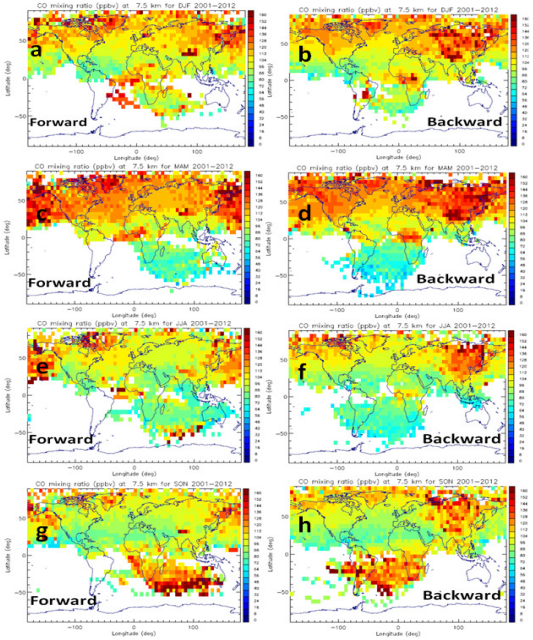

Figure 3. Examples of global distribution of trajectory-mapped MOZAIC-IAGOS CO (ppbv) produced using only backward (right panels) and only forward (left panels) trajectories at 7.5 km a.s.l. The panels: **(a, b)** December–February, **(c, d)** March–May, **(e, f)** June–August and **(g, h)** September–November 2001–2012.

ACPD
15, 29871–29937, 2015

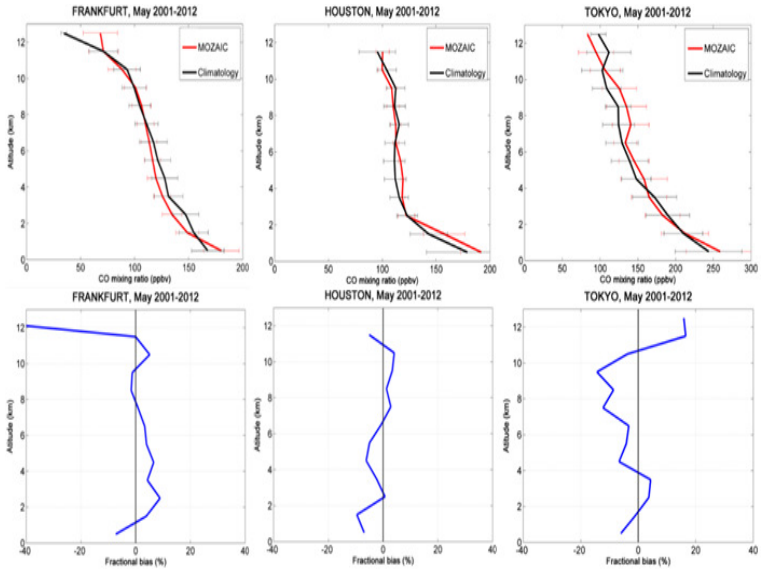

Figure 4. Comparisons of trajectory-mapped MOZAIC-IAGOS CO climatology and MOZAIC-IAGOS profiles at Frankfurt, Germany (left panes), Houston, TX (middle panels), Tokyo, Japan (right panels). The top left, middle and right panels show MOZAIC-IAGOS CO climatology profiles (black) and the corresponding MOZAIC-IAGOS in situ profiles (red) of Frankfurt (Germany), Houston (TX, USA) and Tokyo (Japan) respectively for May 2001–2012. The climatology profiles for each location were produced by excluding data from that location, but using all other MOZAIC-IAGOS data. The horizontal error bar half-length is twice the standard error of the mean (equivalent to 95 % confidence limits on the averages when the number of data points is large). Bottom left, middle and right panels indicate the relative difference [*2(Clim-MOZAIC)/(Clim + MOZAIC)*], expressed in %, between the trajectory-mapped MOZAIC-IAGOS climatology and MOZAIC-IAGOS in situ profiles from Frankfurt (Germany), Houston (USA) and Tokyo (Japan) respectively for May 2001–2012. The actual MOZAIC-IAGOS profiles are labeled as MOZAIC, while the profiles from trajectories without input from the airport station being tested are labeled as Climatology.

ACPD
15, 29871–29937, 2015

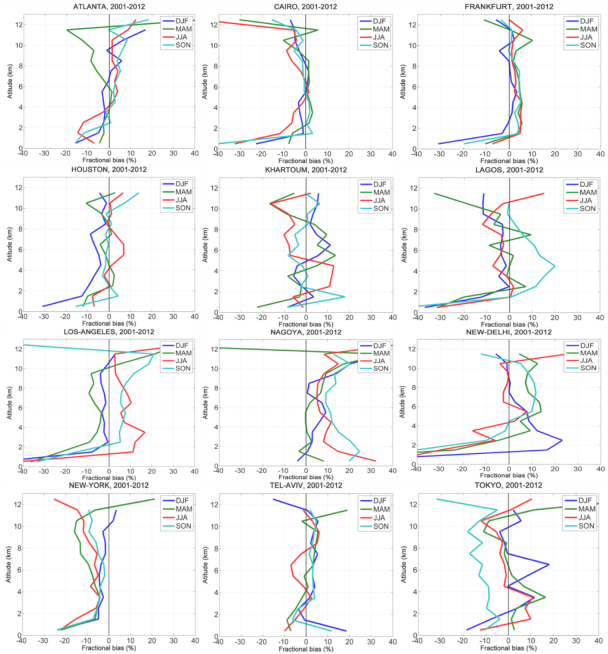

Figure 5. Similar to Fig. 4 (lower panels) but for the seasonal mean biases between trajectory-mapped and MOZAIC-IAGOS in situ profiles for the period from 2001 to 2012. In each panel, different colors indicate different seasons: December–February (blue), March–May (green), June–August (red) and September–November (cyan). The selected airports are representative of different meteorological and source conditions across the globe.

ACPD
15, 29871–29937, 2015

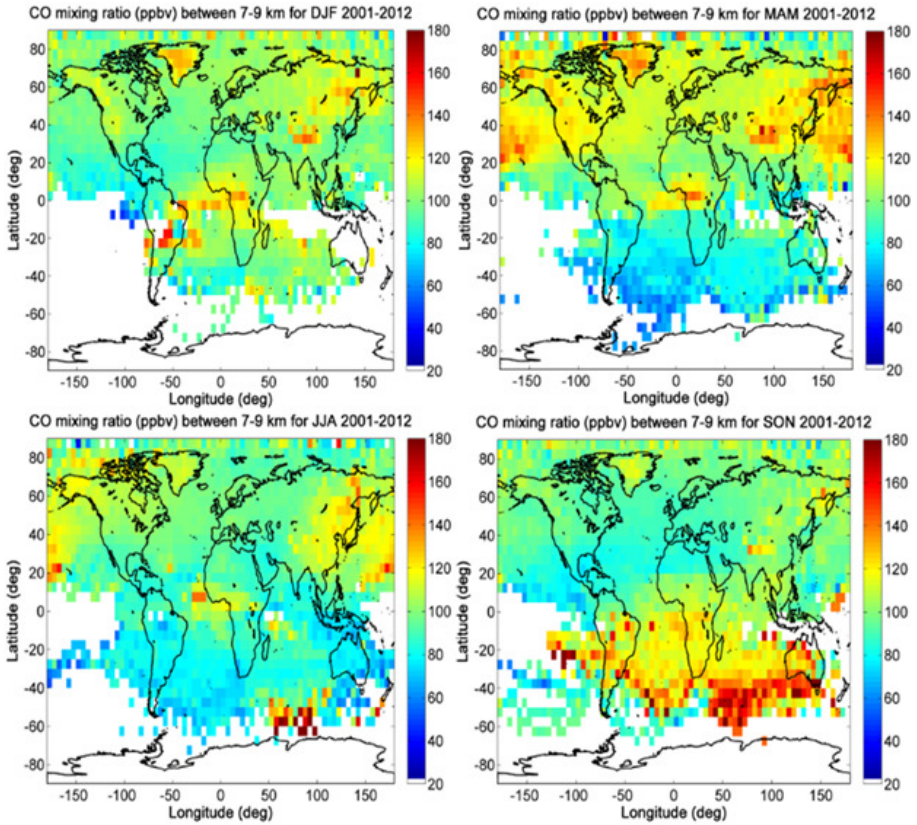

Figure 6. Global distribution of seasonal mean trajectory-mapped MOZAIC-IAGOS CO between 7–9 km altitudes a.s.l. for the period from 2001 to 2012. Panels **(a–d)** show the seasonal mean of CO for December–February, March–May, June–August and September–November, respectively.

ACPD
15, 29871–29937, 2015

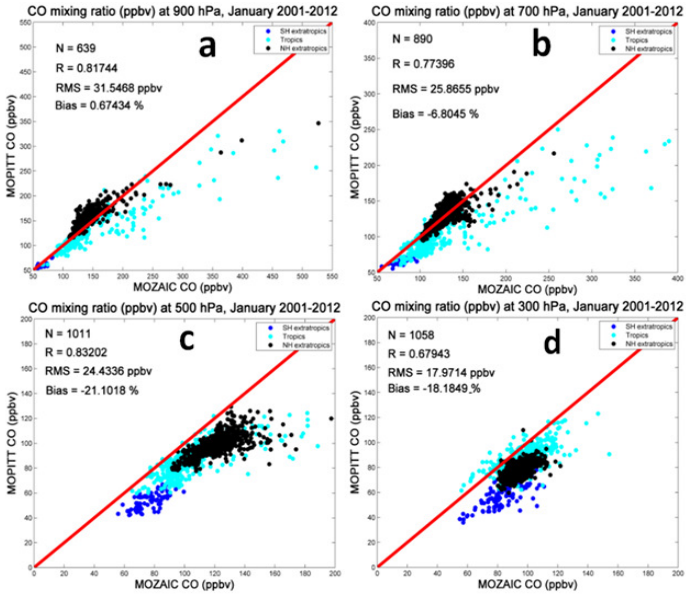

Figure 7. Comparison results for January 2001–2012. MOPITT CO retrievals at 900 **(a)**, 700 **(b)**, 500 **(c)** and 300 hPa **(d)** are plotted against trajectory-mapped MOZAIC-IAGOS CO climatology profiles that have been transformed using the MOPITT averaging kernels and a priori data. The red line is the 1 : 1 line, the blue line is the line of best fit, *N* denotes the total number of data points, *R* is the correlation coefficient, RMS is root mean square error in ppbv and *Bias* is the relative bias between them in %. In each panel, the different color dots show for latitude bands: tropics (cyan), NH extratropics (black) and SH extratropics (blue). In this study, we have used the monthly MOPITT V6 L3 TIR/NIR daytime product.

ACPD
15, 29871–29937, 2015

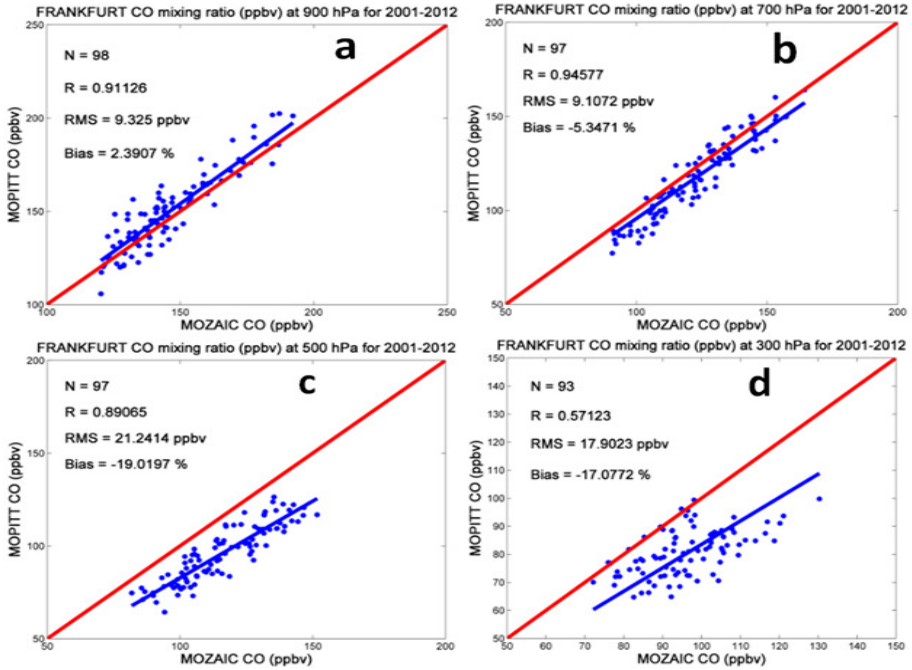

Figure 8. Same as Fig. 7 but MOPITT CO retrievals at 900 **(a)**, 700 **(b)**, 500 **(c)**, and 300 hPa **(d)** are plotted against MOZAIC-IAGOS CO in situ profiles that have been transformed using the MOPITT averaging kernels and a priori data. The in situ profiles are monthly mean from 2001–2012 (Frankfurt, Germany). Outliers (CO mixing ratios more than 1.5 standard deviations from the mean at each pressure level) have been removed, which improves the correlation coefficient at 300 hPa but makes no significant change in other derived parameters.

ACPD
15, 29871–29937, 2015

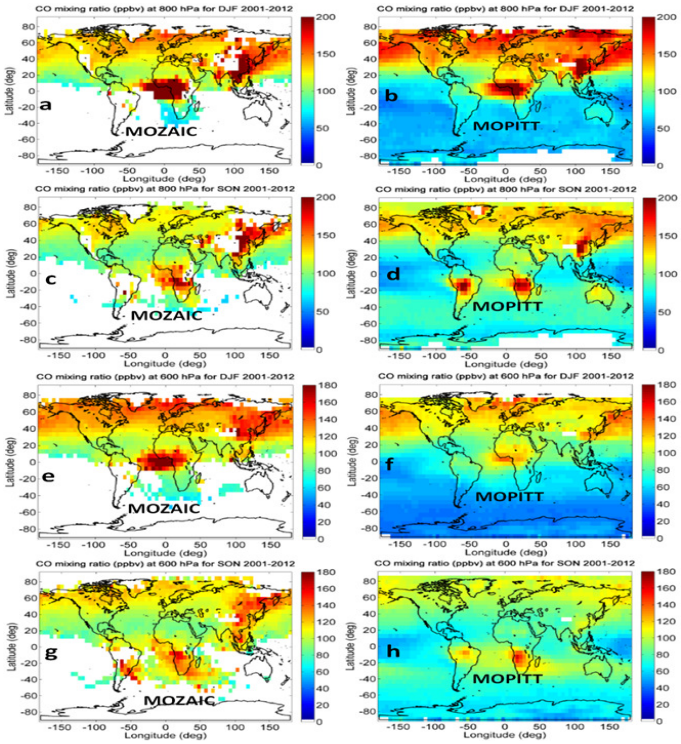

Figure 9. Global distribution of the seasonal mean trajectory-mapped MOZAIC-IAGOS CO climatology (left panels), after transformation with the MOPITT a priori profiles and averaging kernels matrix, and MOPITT CO retrievals (right panels) CO mixing ratio (ppbv) as a function of latitude and longitude at 800 **(a–d)** and 600 hPa **(e–h)** pressure levels. Data are binned at $5^{\circ} \times 5^{\circ}$ in latitude and longitude for the period from 2001–2012. The CO mixing ratios shown in panels: **(a, b)** at 800 hPa for DJF, **(c, d)** at 800 hPa for SON, **(e, f)** at 600 hPa for DJF and **(g, h)** at 600 hPa for SON.

ACPD
15, 29871–29937, 2015

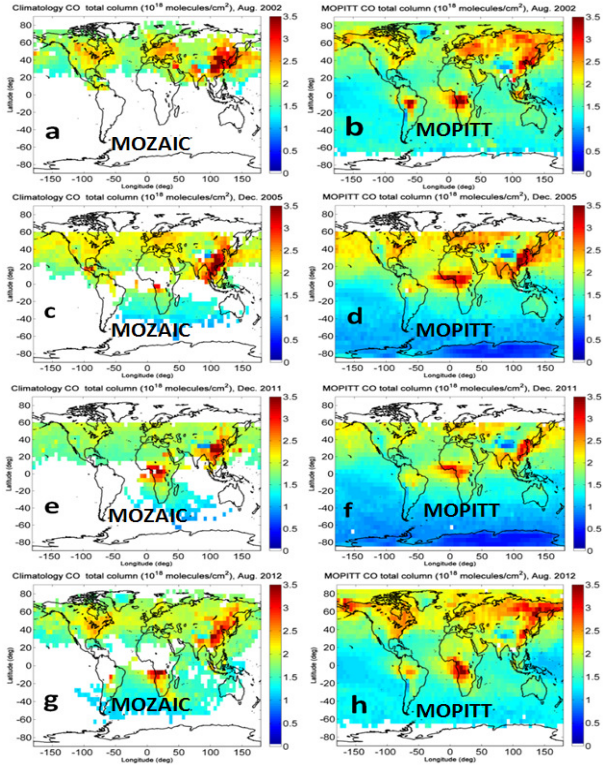

Figure 10. Global total column CO from the transformed trajectory-mapped MOZAIC-IAGOS climatology and MOPITT data for August 2002, December 2005, December 2011 and August 2012. Data are averaged in 5° × 5° latitude–longitude bins.

ACPD
15, 29871–29937, 2015

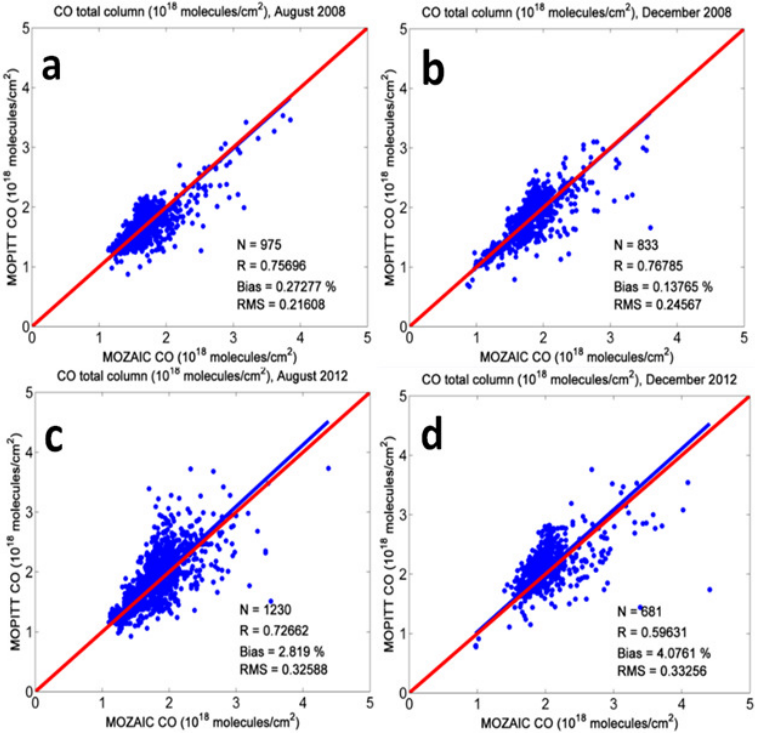

Figure 11. Global MOPITT CO column retrievals vs. transformed trajectory-mapped MOZAIC-IAGOS CO climatology column for the months and years shown above. The mean difference in %, [*2(MOPITT-Clim)/(Clim + MOPITT)*], is calculated for each pixel and then averaged over all pixels. The red line is the 1 : 1 line and the correlation coefficient (R), total number of data points (N) and root mean square error (RMS) are given.

ACPD
15, 29871–29937, 2015

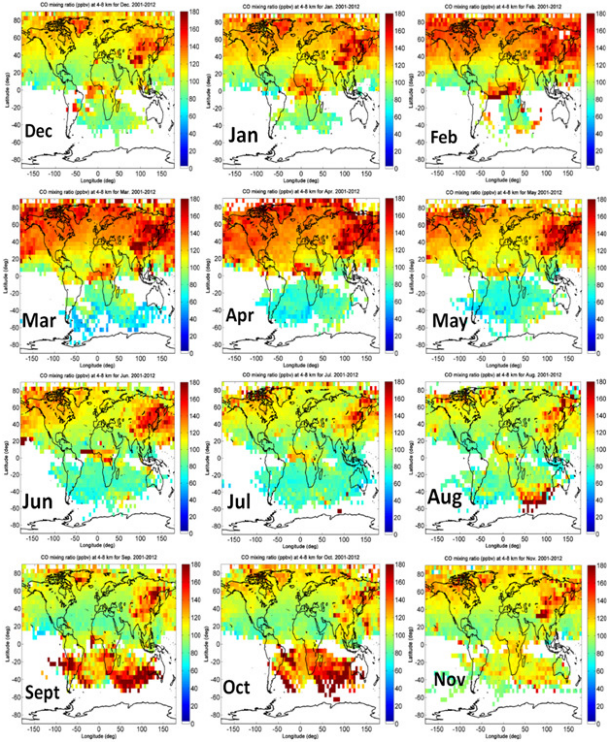

Figure 12. Global monthly mean CO distribution from the trajectory-mapped MOZAIC-IAGOS CO VMR as a function of latitude and longitude for January–December 2001–2012 and altitudes between 4–8 km a.s.l. The data were averaged with a bin size of 5° × 5° latitude and longitude.

ACPD
15, 29871–29937, 2015

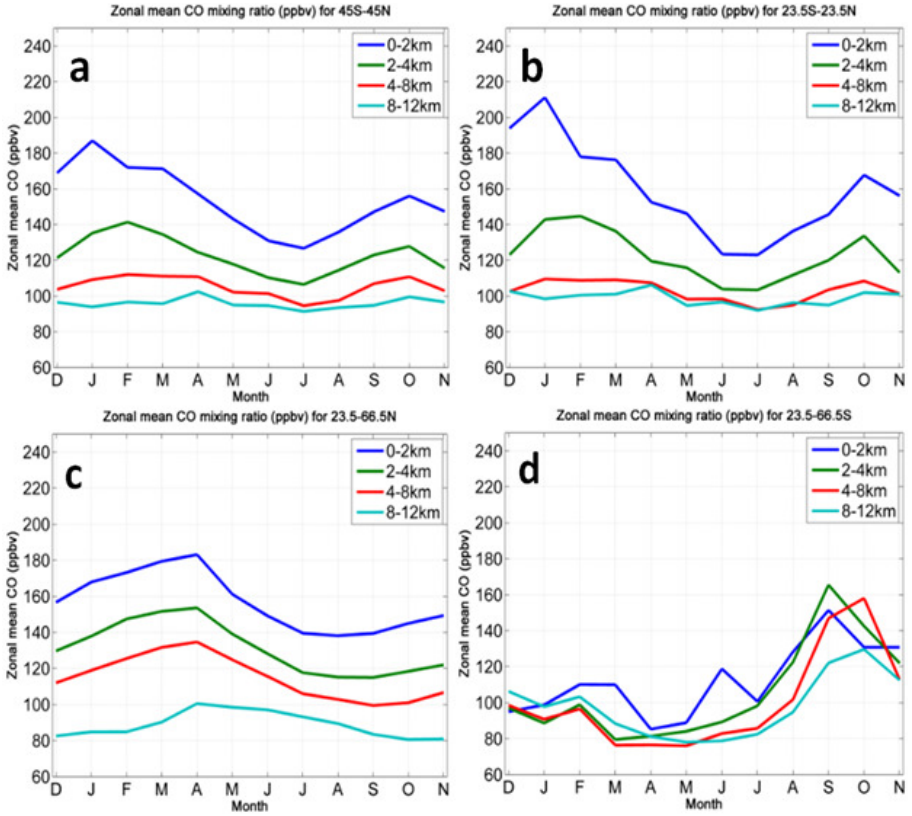

Figure 13. Zonally averaged monthly variation of CO for latitude bands 45° S–45° N **(a)**, 23.5° S–23.5° N **(b)**, 23.5–66.5° N **(c)** and 23.5–66.5° S **(d)**. Monthly mean CO VMRs were calculated for the period 2001–2012, for altitude ranges 0–2, 2–4, 4–8 and 8–12 km a.s.l. The abscissa is monthly mean of CO covered during 2001–2012.

ACPD
15, 29871–29937, 2015

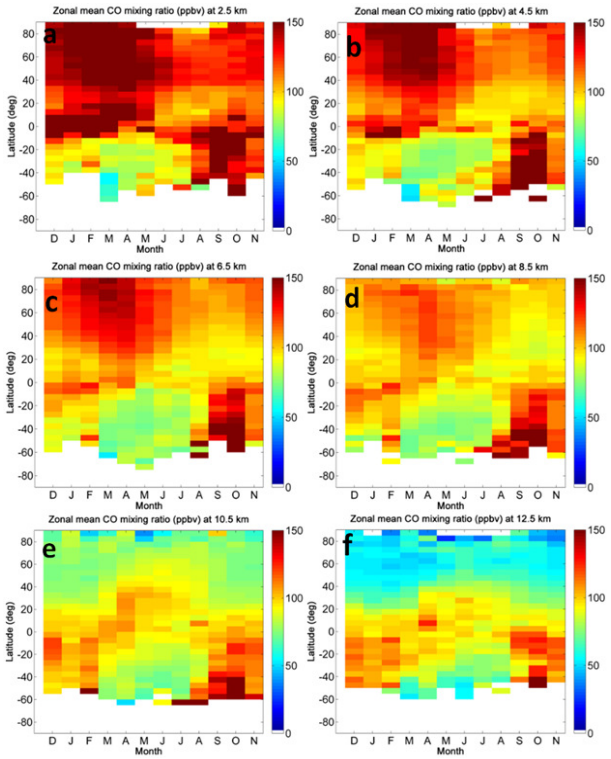

Figure 14. Seasonal variation of zonal monthly mean trajectory-mapped MOZAIC-IAGOS CO climatology at 2.5 **(a)**, 4.5 **(b)**, 6.5 **(c)**, 8.5 **(d)**, 10.5 **(e)** and 12.5 **(f)** altitudes a.s.l. for the period 2001–2012. The zonal mean data are averaged in 5° latitude intervals.

ACPD
15, 29871–29937, 2015

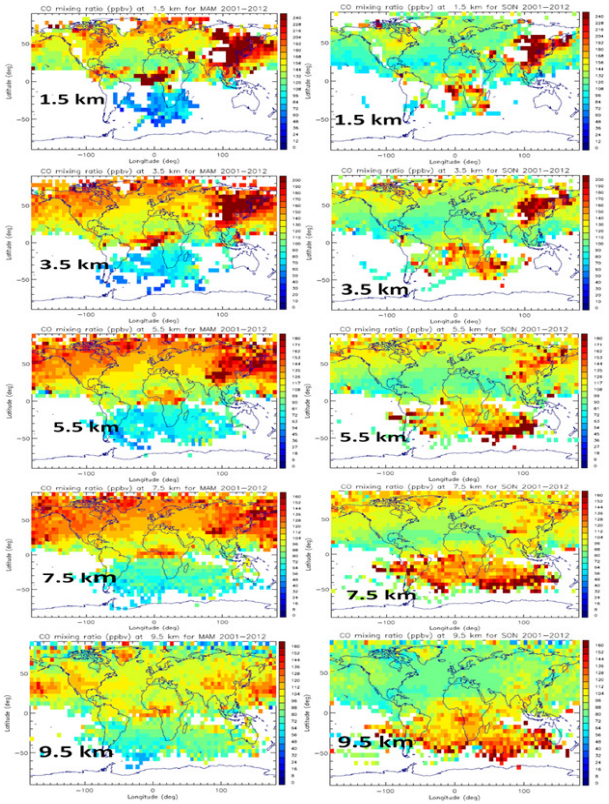

Figure 15. Global distribution of seasonal (the NH spring and fall) mean trajectory-mapped MOZAIC-IAGOS CO climatology as a function of latitude and longitude for altitudes 1.5, 3.5, 5.5, 7.5 and 9.5 km a.s.l. The left and right columns show average CO VMRs for March–April–May and September–October–November 2001–2012. The data are averaged with a bin size of 5° × 5° latitude and longitude.

ACPD
15, 29871–29937, 2015

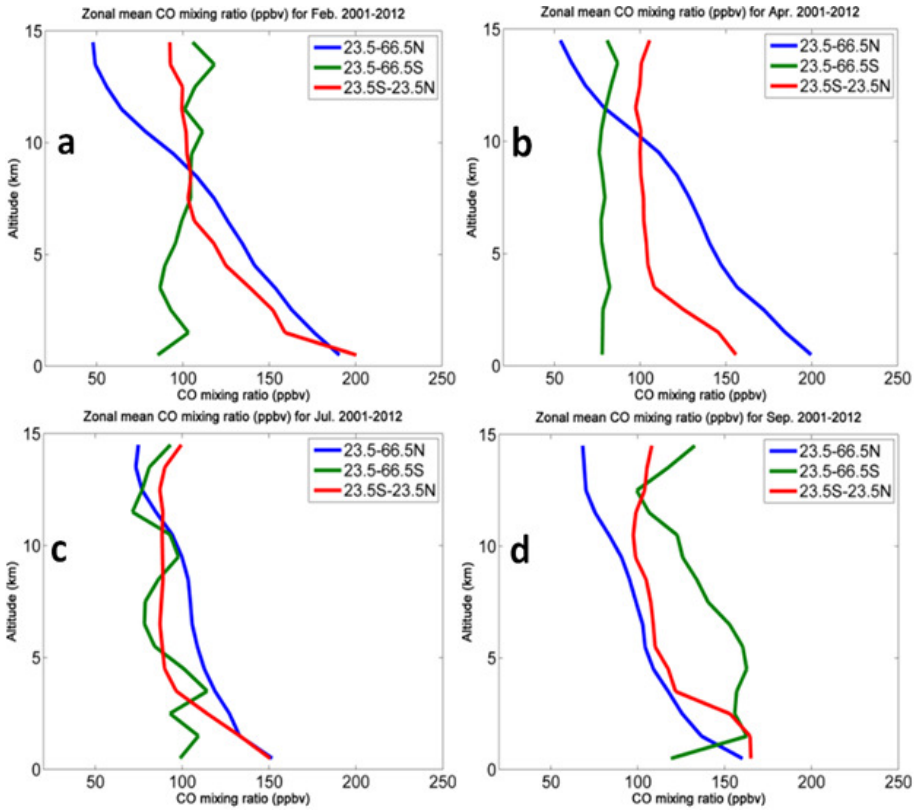

Figure 16. Monthly mean profiles of CO from the trajectory-mapped MOZAIC-IAGOS CO climatology for February **(a)**, April **(b)**, July **(c)** and September **(d)** averaged for 2001–2012. The different colors represent CO mean for latitude bands 23.5–66.5° N (blue), 23.5–66.5° S (green) and 23.5° S-23.5° N (red).

ACPD
15, 29871–29937, 2015

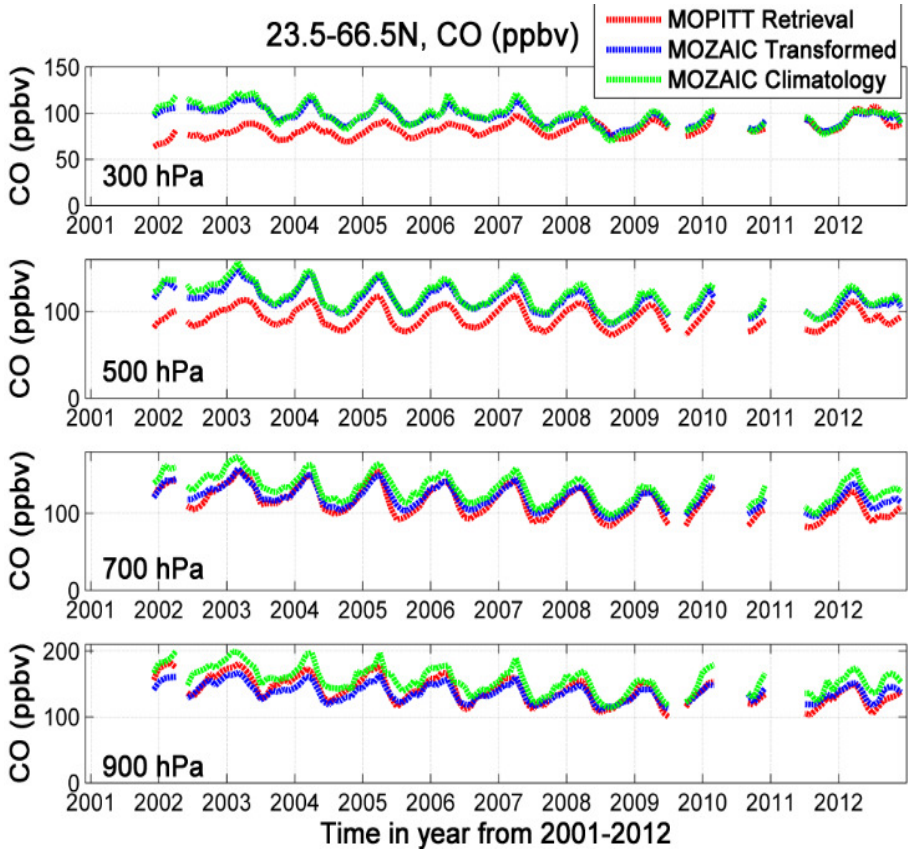

Figure 17. Zonally averaged time series of monthly mean CO VMR as measured by MOPITT CO retrievals and the trajectory-mapped MOZAIC-IAGOS CO climatology (transformed and untransformed) using MOPITT's averaging kernels for the latitude band 23.5–66.5° N.

ACPD
15, 29871–29937, 2015

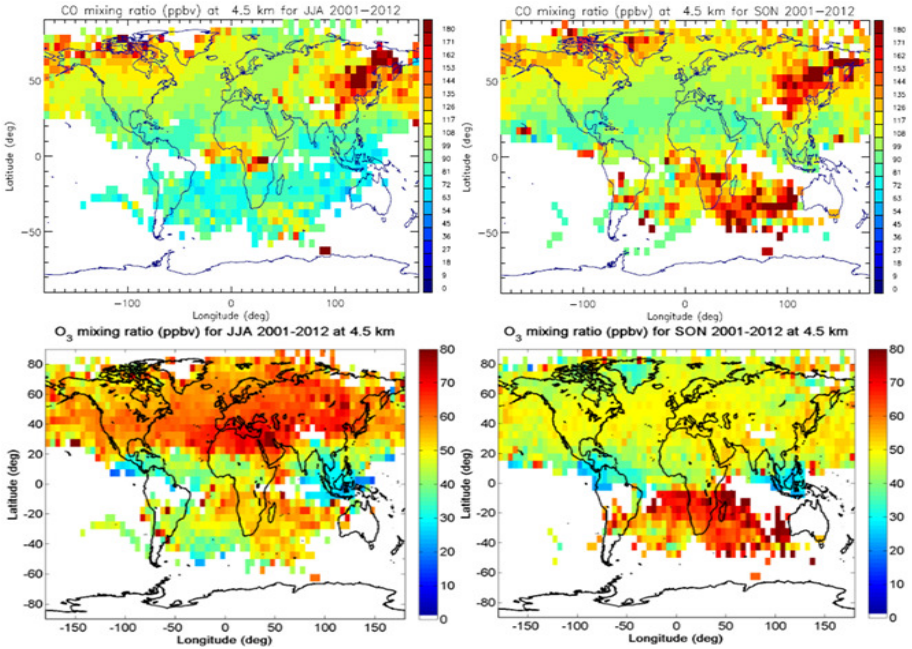

Figure 18. Global distribution of seasonal (NH winter and fall) mean concentrations of O_3 and CO from the trajectory-mapped MOZAIC-IAGOS climatologies as a function of latitude and longitude at 4.5 km altitude a.s.l. The data are binned on a 5° × 5° latitude and longitude grid.

ACPD
15, 29871–29937, 2015

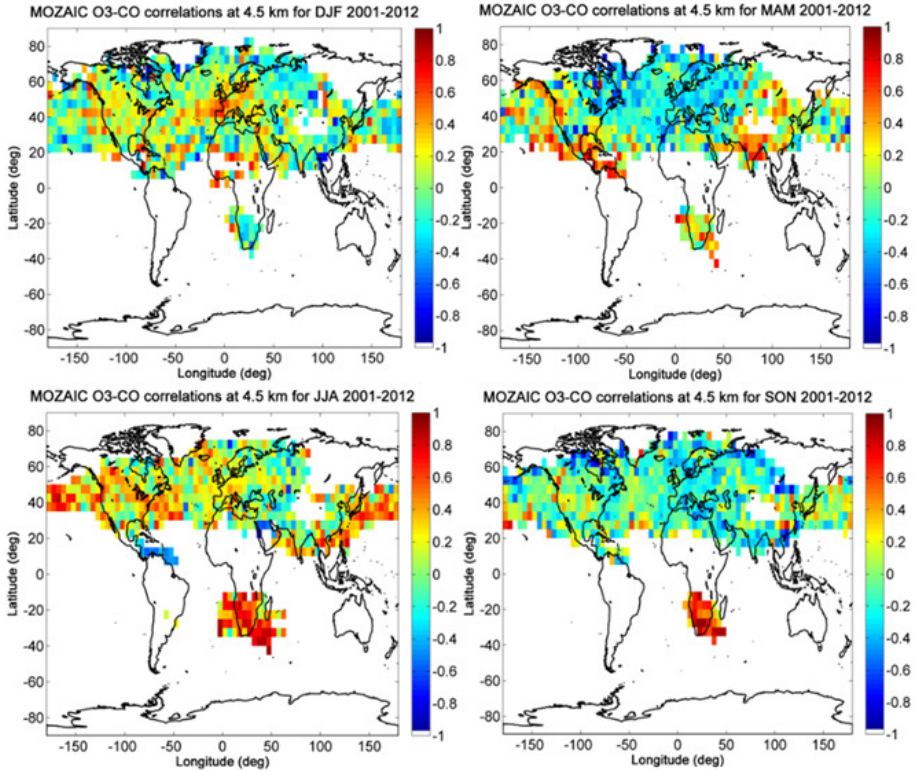

Figure 19. O_3–CO correlation coefficients of seasonal means for 2001–2012 from the trajectory-mapped MOZAIC-IAGOS measurements at 4.5 km altitude a.s.l. The top left, top right, bottom left and bottom right panels are the O_3–CO correlation coefficients for December–February, March–May, June–August and September–November, respectively.

ACPD
15, 29871–29937, 2015

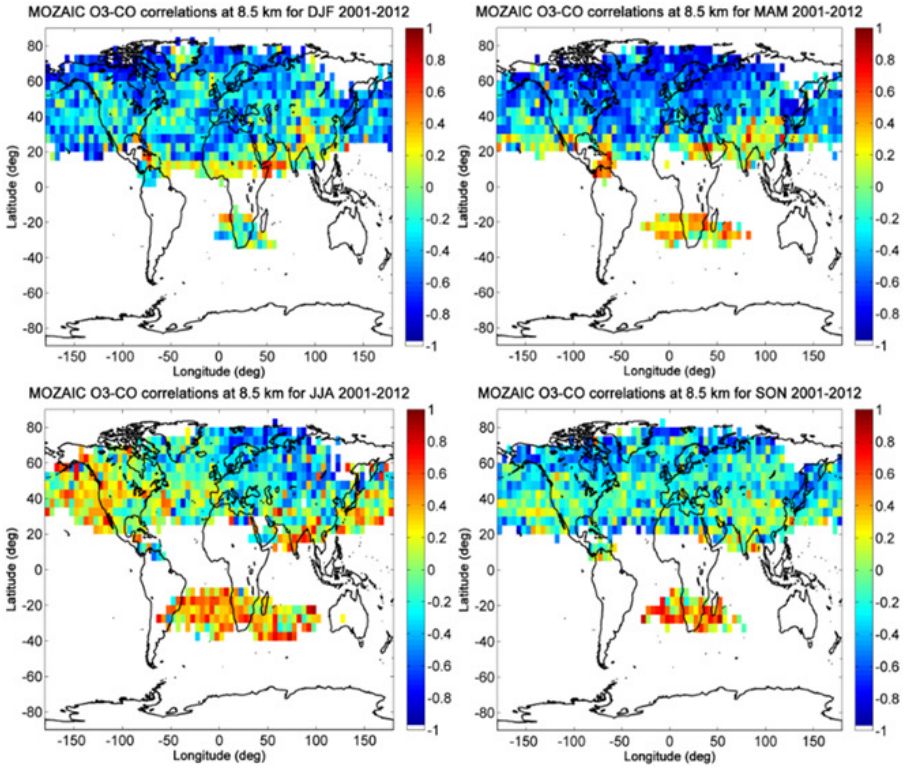

Figure 20. Same as Fig. 19 but for an altitude of 8.5 km a.s.l.

ACPD
15, 29871–29937, 2015

Trajectory-mapped MOZAIC-IAGOS CO climatology

M. Osman et al.

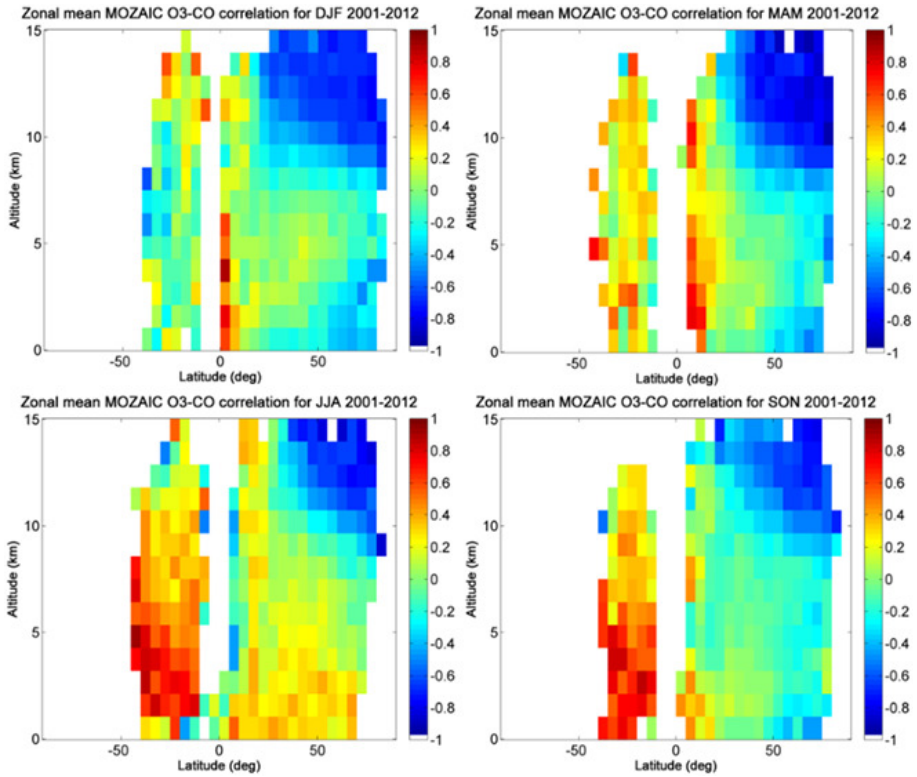

Figure 21. Latitude-altitude cross-section of zonal seasonal means of the O_3–CO correlation coefficients for 2001–2012 from the trajectory-mapped MOZAIC-IAGOS CO and O3 climatologies. The top left, top right, bottom left and bottom right panels are the O_3–CO correlation coefficients for December–February, March–May, June–August and September–November, respectively.

ACPD
15, 29871–29937, 2015